Available online at www.sciencedirect.com
SCIENCE DIRECT®
Journal of Computational Physics 213 (2006) 629–658
JOURNAL OF COMPUTATIONAL PHYSICS
www.elsevier.com/locate/jcp

A wave propagation method for hyperbolic systems on the sphere

James A. Rossmanith *

Department of Mathematics, University of Michigan, 530 Church Street, Ann Arbor, MI 48109-1043, USA

Received 26 August 2004; received in revised form 24 August 2005; accepted 27 August 2005
Available online 7 October 2005

Abstract

Presented in this work is an explicit finite volume method for solving general hyperbolic systems on the surface of a sphere. Applications where such systems arise include passive tracer advection in the atmosphere, shallow water models of the ocean and atmosphere, and shallow water magnetohydrodynamic models of the solar tachocline. The method is based on the curved manifold wave propagation algorithm of Rossmanith, Bale, and LeVeque [A wave propagation algorithm for hyperbolic systems on curved manifolds, J. Comput. Phys. 199 (2004) 631–662], which makes use of parallel transport to approximate geometric source terms and orthonormal Riemann solvers to carry out characteristic decompositions. This approach employs TVD wave limiters, which allows the method to be accurate for both smooth solutions and solutions in which large gradients or discontinuities can occur in the form of material interfaces or shock waves. The numerical grid used in this work is the cubed sphere grid of Ronchi, Iacono, and Paolucci [The 'cubed sphere': a new method for the solution of partial differential equations in spherical geometry, J. Comput. Phys. 124 (1996) 93–114], which covers the sphere with nearly uniform resolution using six identical grid patches with grid lines lying on great circles. Boundary conditions across grid patches are applied either through direct copying from neighboring grid cells in the case of scalar equations or 1D interpolation along great circles in the case of more complicated systems. The resulting numerical method is applied to several test problems for the advection equation, the shallow water equations, and the shallow water magnetohydrodynamic (SMHD) equations. For the SMHD equations, we make use of an unstaggered constrained transport method to maintain a discrete divergence-free magnetic field.

Keywords: Finite volume methods; Cubed sphere; Advection equation; Shallow water equations; Shallow water magnetohydrodynamic equations

1. Introduction

An important goal in large-scale geophysical fluid dynamics is to accurately simulate fluid flow on the surface of a rotating planet. For many years, the dominant numerical method in large-scale atmospheric flows

* Present address: Department of Mathematics, University of Wisconsin-Madison, 480 Lincoln Drive, Madison, WI 53706-1388, USA. Tel.: +1 608 262 3852; fax: +1 608 263 8891.
E-mail address: rossmani@math.wisc.edu.

0021-9991/$ - see front matter
doi:10.1016/j.jcp.2005.08.027

was the spectral method [9,53]; recent developments have seen the implementation of local methods such as finite difference (e.g. [41,49]), compact finite difference (e.g. [45,58]), finite volume (e.g. [25,26,56]), and finite element methods (e.g. [11,21]). Furthermore, two general strategies for obtaining more accurate and efficient numerical methods have recently been applied to large-scale atmospheric models:

1. *p*-adaption: development of high-order discontinuous-Galerkin [23,44,43] and spectral element methods [18,22,24], which allow the order of the scheme to adapt, either dynamically or statically, to features in the solution;
2. *h*-adaption: development of adaptive mesh refinement (AMR) techniques, which allow for more grid points to placed in regions where the numerical solution would otherwise be inaccurate. Unlike the *p*-adaption strategy, *h*-adaption is often built on "lower" order methods (i.e., second and third order) [5,8,30,31].

In the current work, we follow the second strategy of developing lower-order methods, with the aim to develop AMR capabilities in future work. The main reason for pursuing lower-order methods is that we are particularly interested in developing a scheme that is accurate simultaneously for smooth flows and for flows in which large gradients or discontinuities such as material interfaces or shock waves can form. Others who have considered such schemes include Blikberg [8], Hubbard and Nikiforakis [30], Jablonowski [31], Lanser et al. [34], and Liska and Wendroff [40].

Numerical schemes that make use of total variation diminishing (TVD) limiters such as LeVeque's wave propagation method [37] have been shown to be accurate on a wide range of solution regimes and application problems (e.g. gas dynamics [33], acoustics [16,17], elasticity and plasticity [15,35,38,39], combustion and detonation waves [27,28], relativistic hydrodynamics [2], and numerical relativity [4,29]). Furthermore, it has been shown that, even on smooth solutions, limiters can sometimes improve the accuracy of a simulation by reducing phase errors (see Fig. 6.3 on p. 105 of LeVeque [39]). Rossmanith et al. [51] recently developed an extension of the wave propagation scheme [37] to curved manifolds. The main goal of this work is to extend this method so that it can be applied to flow on a sphere.

In addition to selecting a numerical method, one must also choose a numerical grid that covers the sphere. Many strategies have been proposed including numerical grids based on triangles (e.g. [5,59]), rectangles (e.g. [41,49]), and hexagons (e.g. [25,26,56]). The methods we propose in this work are based on logically Cartesian grids (i.e., rectangles), and rely on fully explicit time stepping strategies. Therefore, we will make use of the cubed sphere grid of Ronchi et al. [49], which divides the sphere into six grid "patches" of nearly uniform resolution. How to obtain accurate numerical results across the grid interfaces is a major thrust of this paper. This grid is discussed in detail in Section 3.

The resulting numerical method is applied to the following three hyperbolic systems:

1. *The advection equation:* a model for tracer transport such as various kinds of pollutants in the atmosphere.
2. *The shallow water equations:* a hydrostatic, single-layer model of the ocean or atmosphere.
3. *The shallow water magnetohydrodynamic (SMHD) equations:* a hydrostatic, single-layer model of the solar tachocline.

We present the general numerical scheme in Section 4.1, while implementation details for the above three systems are presented in Sections 4.2–4.4, respectively. Presented in 4.2 is a curved manifold extension of LeVeque's [36] treatment of the velocity field, which guarantees that the velocity field satisfies a discrete divergence-free condition. Presented in 4.4 is a curved manifold extension of the constrained transport method of Rossmanith [50], which guarantees that the magnetic field satisfies a discrete divergence-free condition. Simulation results on several test cases are shown in Section 5.

2. Notation

A summary of the notation that will be used throughout this paper can be found in Table 1. Unless otherwise noted, summation is implied whenever the same index appears as both a subscript and a superscript, e.g.

Table 1
Summary of notation

Symbol	Description
$\mathscr{M}$	A general curved manifold, $\mathscr{M} \in \mathbb{R}^3$
(x^1, x^2)	Coordinates that parameterize the manifold $\mathscr{M}$
$\vec{u}$, u^k	Vector, kth component
$\underset{\leftarrow}{u}^{\hat{k}}$	kth component of vector $\vec{u}$ after it has been orthonormalized
$\underset{\leftrightarrow}{\mathscr{T}}$, $\mathscr{T}^{mn}$	Tensor, mnth component
G, G_{mn}, G^{mn}	Metric tensor, mnth component, mnth component of inverse
$\sqrt{G}$	Square root of the determinant of the metric tensor
$\frac{\partial}{\partial x^k}$	Derivative in the kth coordinate direction
Γ^k_{mn}	kmnth Christoffel symbol
$N \times N \times 6$	A cubed sphere with $N \times N$ resolution on each grid, $N = 90 \iff \approx 1^\circ$ resolution ≈ 111 km resolution

$$\Gamma^m_{nk}\mathscr{T}^{kn} = \sum_n \sum_k \Gamma^m_{nk}\mathscr{T}^{kn}.$$

Our notation is consistent with that of Misner et al. [42].

3. The cubed sphere grid

In this work, we consider the "cubed sphere" grid mapping first introduced by Sadourny [52]; this mapping takes points on a sphere to the six faces of a cube. Sadourny [52] applied a finite difference method to solve the shallow water equations on this grid, but concluded that further work was needed to reduce inaccuracies near the internal boundaries (i.e., edges of the cube). As a result of this conclusion and because during this time spectral methods were shown to produce accurate results with good efficiency [9], very little attention was given to the cubed sphere grid for more than two decades. It was not until the mid-1990s that the global dynamics community found renewed interest in the approach of Sadourny [52].

Cubed sphere grids fall into two main categories: conformal [48] and non-conformal [48,49]. The conformal cubed sphere mapping preserves the orthogonality of the spherical coordinate system, thereby minimizing the additional geometric terms that appear in the underlying partial differential equations. The disadvantage with this approach is that the grid cell area is very non-uniform, yielding grid cells that near the internal boundaries are much smaller than those in the interior [48]. For most explicit time stepping methods this means that the time step will be severely restricted by the small cells, and therefore, we will not consider this grid mapping in the current investigation. We should also note that through a variational technique, Purser and Rancic [47] were able to obtain more uniform grids by allowing the grid transformation to become slightly non-conformal.

The non-conformal approach of Ronchi et al. [49] was instead aimed at generating a grid mapping that is nearly uniform and expressible in terms of analytic formulas. In this approach the sphere is divided into six equal regions, each generated by taking grid points to be the intersection of great circles passing through the "north" and "south" poles with great circles passing through the "east" and "west" poles relative to that region (see Fig. 1(a)). Doing this for each region generates six equal grids that cover the entire sphere without overlap. This mapping is illustrated in Fig. 2. Ronchi et al. [49] showed that the area ratio of the smallest to the largest grid cell converges to $\sqrt{2}/2 \approx 0.7071$ as the grid resolution goes to infinity, and furthermore, for a finite grid resolution this ratio is always larger than $\sqrt{2}/2$ (see Fig. 1(b)). Note that the smallest grid cells occur at the interface between two grid patches.

3.1. Grid transformations

The standard spherical coordinates are denoted by (λ, θ), where $\lambda \in [-\pi, \pi]$ is the longitude, $\theta \in [-\pi/2, \pi/2]$ is the latitude. Throughout this paper we scale all variables so that the radius of the sphere is always $r = 1$. On each of the six grid patches we define the following coordinates:

$$(x^1, x^2) \in \left[-\frac{\pi}{4}, \frac{\pi}{4}\right] \times \left[-\frac{\pi}{4}, \frac{\pi}{4}\right]$$

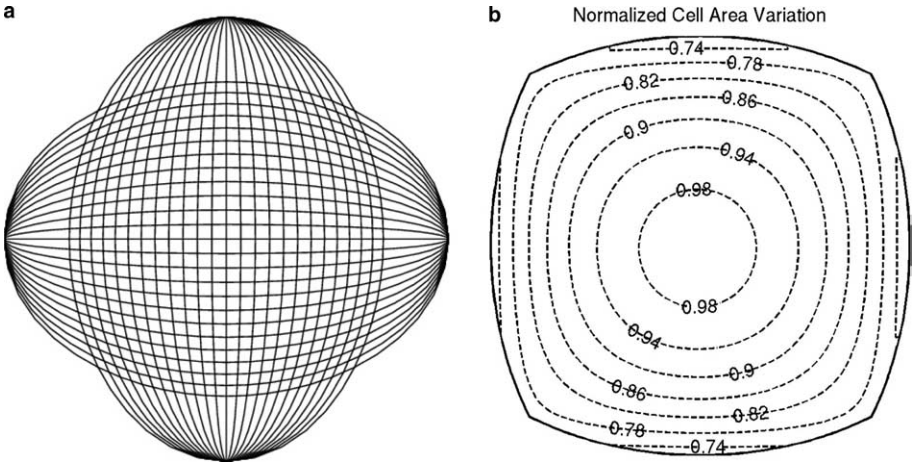

Fig. 1. (a) A single grid patch is constructed by taking the intersection of a set of angularly equidistant great circles clamped down at the "north" and "south" poles relative to that patch with a set of angularly equidistant great circles clamped down at the "east" and "west" poles relative to that patch. (b) A plot of the cell area normalized by the largest grid cell.

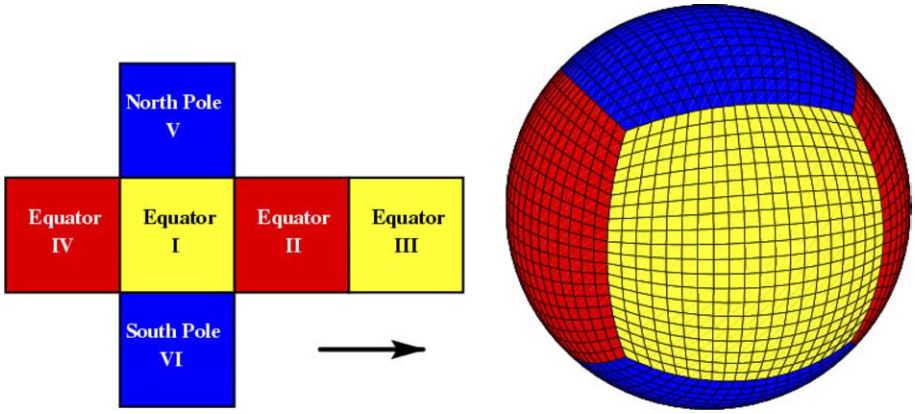

Fig. 2. The cubed sphere grid mapping maps the six faces of a cube to the surface of a sphere. The specific mapping shown here is non-orthogonal and generates a grid that varies less than 30% in grid cell area.

along with the following Jacobian, J, that maps vectors expressed in the coordinate basis of (x^1, x^2) to vectors expressed in the coordinate basis of (λ, θ);

$$\begin{bmatrix} u^\lambda \\ u^\theta \end{bmatrix} = J \begin{bmatrix} u^1 \\ u^2 \end{bmatrix} = \begin{bmatrix} \frac{\partial \lambda}{\partial x^1} & \frac{\partial \lambda}{\partial x^2} \\ \frac{\partial \theta}{\partial x^1} & \frac{\partial \theta}{\partial x^2} \end{bmatrix} \begin{bmatrix} u^1 \\ u^2 \end{bmatrix}. \tag{1}$$

The grid transformations, $\lambda = \lambda(x^1, x^2)$ and $\theta = \theta(x^1, x^2)$, can be found in Ronchi et al. [49]. The metric on each grid patch can be expressed as follows:

$$\overleftrightarrow{G} = J^{\mathrm{T}} \overleftrightarrow{G}_{\mathrm{sphere}} J, \tag{2}$$

where the orthogonal metric induced by the standard spherical coordinates is given by

$$\overleftrightarrow{G}_{\mathrm{sphere}} = \mathrm{diag}\left(\cos^2(\theta), 1\right). \tag{3}$$

We note that our definition of the metric tensor $\overleftrightarrow{G}$ differs from the definitions of Ronchi et al. [49] and Nair et al. [43]. In those papers, the metric gives a measure of how distance is measured on the cubed sphere grid relative to the standard *longitude–latitude coordinates*; therefore, these papers use the definition $\overleftrightarrow{G} \equiv J^{\mathrm{T}} J$, without the $\overleftrightarrow{G}_{\mathrm{sphere}}$ in between the Jacobian transpose and the Jacobian. In the numerical scheme we present in this

paper we require definition (2), which gives us a relative measure of distance between the cubed sphere grid and standard *Cartesian coordinates*. Furthermore, it will often be necessary to compute the distance between two points on the surface the sphere; the shortest distance between two points (λ, θ) and (λ_0, θ_0) is obtained by taking the great circle that passes through both points and then computing the shorter arc length between the two points on the great circle;

$$\mathrm{dist}(\lambda, \theta, \lambda_0, \theta_0) \equiv \arccos\{\cos(\theta)\cos(\theta_0)\cos(\lambda - \lambda_0) + \sin(\theta)\sin(\theta_0)\}. \tag{4}$$

3.2. Boundary conditions

The cubed sphere grid mapping provides us with a nearly uniform grid on the surface of a sphere and eliminates the grid singularities at the poles that are introduced by the latitude–longitude grid. We are now faced with two new difficulties:

1. The underlying metric is non-orthogonal.
2. Artificial boundaries between the six grid patches have been created.

Although the equations are somewhat more complicated in a non-orthogonal coordinate system, the numerical methods that we will introduce in Section 4 work well for general metric tensors. This leaves us only with the second challenge of dealing with the artificial boundaries between grid patches.

Conceptually, we can think of solving the governing partial differential equation on each of the six grid patches as separate problems. Each grid patch has its own interior grid cells, its own (x^1, x^2) coordinate system, and at least two layers of *ghost cells* as required by the wave propagation method [39]. Information is passed between grid patches by placing the appropriate boundary conditions into the ghost cells. Note that the orientation (i.e., the labeling of the coordinate directions x^1 and x^2) may change from one grid patch to the next. A grid cell on a general curved manifold is defined by an index (i,j), a grid center (x^1_i, x^2_j), and a solution value (Q_{ij}). Before we can place solution value information into the ghost cells, we must first decide on how to define the geometry of the ghost cells. Two reasonable choices for the ghost cell geometry are the following:

Method 1: Let the ghost cells have the same shape as the grid cells from the neighboring grid patch and directly copy solution values into these cells.

Method 2: Extend the coordinate lines of the current grid patch into its neighboring grid patches, then interpolate information from the neighboring patches into these extended cells. In this work we use standard linear interpolation, and because of the geometry of the extended cells, we only need one-dimensional interpolation in each layer of ghost cells [49].

These two methods are illustrated in Fig. 3. The first method is attractive because the ghost cells and the neighboring grid patch identically match, meaning that no interpolation is required to place solution values (Q_{ij}) into the ghost cells. This approach works well for scalar conservation laws (e.g. advection). Method 1 fails for more general hyperbolic systems, however, since vector quantities on either side of a grid interface are represented in different coordinate systems, and one cannot to solve 1D coordinate Riemann problems between these data. Instead, for general hyperbolic systems we use Method 2 to extend the grid patches and obtain ghost cell data via interpolation. The overlap is such that only one-dimensional interpolation is required along the great circle lines (see [49]). This technique of interpolating onto overlaping grids is a special case of the overlapping grid technique developed by Chessire and Henshaw [12].

In this work, we will make use of both of the above methods depending on the equations that are being solved:

1. The advection equation: Method 1 with two layers of ghost cells.
2. The shallow water equations: Method 2 with two layers of ghost cells.
3. The shallow water magnetohydrodynamic equations: Method 2 with three layers of ghost cells.

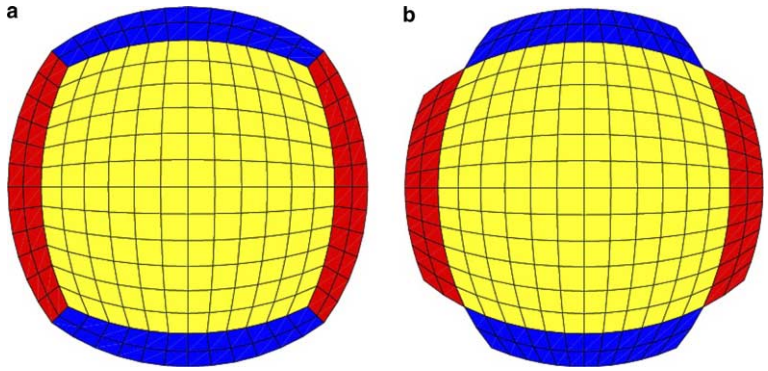

Fig. 3. Two types of boundary conditions for the six sphere patches: (a) Ghost cells are the same as grid cells on neighboring patches; no interpolation is required to obtain the solution values (Q_{ij}) in these ghost cells. (b) Ghost cells are obtained by extending the current grid onto the neighboring patch. Solution values (Q_{ij}) are placed into these ghost cells by one-dimensional interpolation along great circle lines.

The advection equation can be described entirely by two scalars: the concentration $(q(\vec{x},t))$ and the stream-function $(\psi(\vec{x},t))$. Because scalars are coordinate independent, Method 1 can be used in this situation. Furthermore, the use of Method 1 will guarantee the numerical conservation of $q(\vec{x},t)$ across grid patches. Two layers of ghost cells are required in order to apply wave limiters to the information entering through the grid interfaces [39].

In solving the shallow water and shallow water magnetohydrodynamic (SMHD) equations we will make use of Method 2. In this case we will lose (mass) conservation across grid interfaces, because at each grid interface we will compute two numerical fluxes. For example, consider two neighboring equatorial grids, which we denote by "left" and "right". At the grid interface, the following two fluxes are computed: F_{l} (flux computed on "left" grid) and F_{r} (flux computed on "right" grid). Although these fluxes sit at the same spatial location, they will in general not be the same, since the data that generated them is different (see Fig. 4). One could remedy this situation by defining a unique flux function at the cell interface in the following way:

$$F_{\text{interface}} = \frac{1}{2}(F_{\mathrm{l}} + F_{\mathrm{r}}). \tag{5}$$

In practice, however, we have found that better results are obtained by not applying (5). We will demonstrate through direct numerical simulations in Section 5 that despite the slight loss of conservation at grid interfaces, the numerical solutions remain accurate. Furthermore, it is shown that shocks can propagate through the grid interfaces without visible accuracy degradation. Finally, we note that despite some conservation loss at the boundaries, the method is still locally conservative away from the boundaries and remains accurate for the

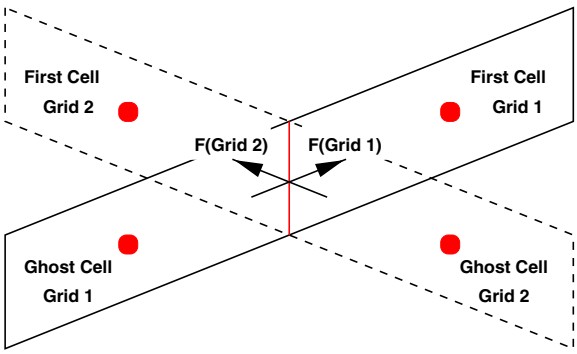

Fig. 4. This figure shows why Method 2 does not conserve mass. Across each grid interface, two different Riemann problems are being solved: one to update the solution on the left grid (Grid 2 in this figure), the other to update the solution on the right grid (Grid 1 in this figure). Since these two Riemann problems use different data, they will in general produce different fluxes. This causes a slight loss of conservation across the grid interface.

purposes of shock-capturing. For other examples of schemes that fail to be conservative in regions of co-dimension one, yet remain accurate across shock waves, see Abgrall and Karni [1].

4. The numerical method

We propose in this section a numerical method for solving the advection, shallow water, and shallow water MHD equations on the surface of a sphere. In particular, we extend the scheme of Rossmanith et al. [51] (RBL for short) so that it can be applied to the multiple grid patch geometry of the cubed-sphere grid. A brief review of the RBL scheme is described in Section 4.1, while additional details for the advection, shallow water, and SMHD equations are provided in Sections 4.2–4.4.

4.1. The RBL wave propagation method

RBL considered, without loss of generality, a generic conservation law on a curved manifold $\mathscr{M} \in \mathbb{R}^3$ consisting of one scalar conserved quantity, the "mass" density ρ, and one vector conserved quantity, the "momentum" density $\vec{\mu}$. We place on $\mathscr{M}$ a coordinate system denoted by (x^1, x^2). In a basis directly tied to this coordinate system (i.e., the *coordinate basis*), the conservation law can be written as follows:

$$\frac{\partial}{\partial t} q(\vec{x}, t) + \frac{1}{\sqrt{G}} \frac{\partial}{\partial x^k} f^k(q, \vec{x}) = \Psi(q, \vec{x}), \tag{6}$$

where

$$q(\vec{x}, t) = \begin{bmatrix} \rho \\ \mu^1 \\ \mu^2 \end{bmatrix}, \quad f^k(q, \vec{x}) = \sqrt{G} \begin{bmatrix} U^k \\ \mathscr{T}^{k1} \\ \mathscr{T}^{k2} \end{bmatrix}, \quad \text{and} \quad \Psi(q, \vec{x}) = \begin{bmatrix} 0 \\ -\Gamma^1_{nk} \mathscr{T}^{kn} \\ -\Gamma^2_{nk} \mathscr{T}^{kn} \end{bmatrix}.$$

In the above expression $\sqrt{G}$ denotes the square root of the determinant of the metric on $\mathscr{M}$, $\vec{U}$ is the "mass" flux vector, $\overleftrightarrow{\mathscr{T}}$ is the "momentum" flux tensor, and Γ^m_{nk} are the Christoffel symbols. The Christoffel symbols can be directly computed by appropriately differentiating the components of the metric tensor (see [51] for the formulas). Superscript indices on vector components denote *contravariant* components, and summation is implied for any index that appears as both a subscript and a superscript. Note that even though $\vec{\mu}$ satisfies the equation of momentum conservation, the individual components of μ are in general not conserved due to the geometric source term Ψ.

Numerically, system (6) can be discretized by first defining on $\mathscr{M}$ a logically Cartesian grid that is made up of $x^1 = \text{constant}$ and $x^2 = \text{constant}$ lines. The resulting grid cells are indexed by (i,j) and the center of each grid cell is denoted by (x^1_i, x^2_j). The grid spacing is denoted as follows:

$$\Delta x^1 = x^1_{i+1} - x^1_i = \text{constant } \forall i,$$
$$\Delta x^2 = x^2_{j+1} - x^2_j = \text{constant } \forall j.$$

The approximate solution at time level $t = t^n$ in grid cell (i,j) is given by

$$Q^n_{ij} \approx \frac{1}{\sqrt{G_{ij}}} \int_{x^1_{i-1/2}}^{x^1_{i+1/2}} \int_{x^2_{j-1/2}}^{x^2_{j+1/2}} \sqrt{G} q(\xi, \eta, t^n) \, \mathrm{d}\xi \, \mathrm{d}\eta, \tag{7}$$

where $x^1_{i-1/2} \equiv x^1_i - \Delta x^1/2$. The approximate solutions are updated using a modified version of the wave propagation method of LeVeque [37];

$$\begin{aligned} Q^{n+1}_{ij} = Q^n_{ij} &- \frac{1}{\sqrt{G_{ij}}} \frac{\Delta t}{\Delta x^1} \left[\mathscr{A}^-_1 \Delta Q_{i+1/2,j} + \mathscr{A}^+_1 \Delta Q_{i-1/2,j} \right] - \frac{1}{\sqrt{G_{ij}}} \frac{\Delta t}{\Delta x^2} \left[\mathscr{A}^-_2 \Delta Q_{i,j+1/2} + \mathscr{A}^+_2 \Delta Q_{i,j-1/2} \right] \\ &- \frac{1}{\sqrt{G_{ij}}} \frac{\Delta t}{\Delta x^1} \left[\widetilde{F}^1_{i+1/2,j} - \widetilde{F}^1_{i-1/2,j} \right] - \frac{1}{\sqrt{G_{ij}}} \frac{\Delta t}{\Delta x^2} \left[\widetilde{F}^2_{i,j+1/2} - \widetilde{F}^2_{i,j-1/2} \right], \end{aligned} \tag{8}$$

where $\mathscr{A}_1^{\pm}\Delta Q$ and $\mathscr{A}_2^{\pm}\Delta Q$ are first-order fluctuations and $\widetilde{F}^1$ and $\widetilde{F}^2$ are second-order corrections. The strategy of the wave propagation method is then to construct all these terms by solving locally valid, one-dimensional, linearized Riemann problems at each cell interface. For example, the 1D Riemann problem at the cell edge $(x^1_{i-1/2}, x^2_j)$ can be written as:

$$\frac{\partial}{\partial t}\left(\sqrt{G}q\right) + \widetilde{A}^1_{i-1/2,j}\frac{\partial}{\partial x^1}q = 0, \tag{9}$$

$$q(x^1, t=0) = \begin{cases} Q^n_{i-1,j} & \text{if } x^1 < x^1_{i-1/2}, \\ Q^n_{ij} & \text{if } x^1 > x^1_{i-1/2}, \end{cases} \tag{10}$$

where

$$\widetilde{A}^1_{i-1/2,j} \approx \frac{\partial f^1}{\partial q}\left(q(\vec{x}_{i-1/2,j}, t), \vec{x}_{i-1/2,j}\right) \tag{11}$$

is an approximate flux Jacobian that is considered to be constant in the Riemann problem. Under the assumption that Eq. (9) is hyperbolic (i.e., $\widetilde{A}^1$ has all real eigenvalues and a complete set of eigenvectors), then the exact solution to (9) and (10) is a set of left and right traveling waves [39]. Fluctuation $\mathscr{A}_1^+\Delta Q$ ($\mathscr{A}_1^-\Delta Q$) is a sum over all the right (left) traveling waves. With only these fluctuations, update (8) is only first-order accurate and stable up to Courant number 1/2. Corrections $\widetilde{F}^1$ and $\widetilde{F}^2$ contain additional terms that are built from the solution to Riemann problems such as (9) and (10). A key feature of these corrections is that because the detailed solution to the linearized Riemann problem is known, we can apply standard total variation diminishing (TVD) limiters to each wave family. This allows us to dynamical switch between a first-order accurate (diffusive) update in regions where the solution has a large gradient (strong waves) and a second-order accurate (dispersive) update in regions where the solution is smooth (weak waves). $\widetilde{F}^1$ and $\widetilde{F}^2$ also contain multidimensional corrections that are obtained from solving additional linearized Riemann problems called *transverse Riemann* problems. These corrections avoid the need for dimensional splitting, yet still produce an update that is stable up to Courant number one. See LeVeque [37] for more details on all these terms.

The RBL wave propagation method follows the strategy outlined above with two important modifications. First, instead of solving linearized Riemann problem (9) and (10) at cell interfaces, RBL solve simpler orthonormal (Cartesian) Riemann problems. The orthonormal Riemann problem has a simpler solution structure, since all metric terms disappear in this description (i.e., the metric tensor becomes the identity matrix). The lost geometric scalings that must be included in the final solution are encoded in orthonormalization and de-orthonormalization pre- and post-processing steps. Second, prior to solving these orthonormal Riemann problems, vectors that are defined at cell centers are moved into a reference frame defined on the cell edge using a geometric concept known as *parallel transport*. RBL showed that parallel transport yields a natural discretization of the geometric source terms that removes the need for operator splitting on these terms. Using this strategy, the RBL scheme has the following properties:

1. The scheme is second-order accurate for smooth solutions and first-order accurate and non-oscillatory in the vicinity of discontinuities.
2. The scheme locally conserves mass, although small conservation errors will occur across grid boundaries when using Method 2 (described in previous section) to handle boundary conditions across grid patches.
3. If the scheme is used to update an equation with M variables on an $N \times N$ grid, the cost of the RBL algorithm is $\mathcal{O}(M^2N^2)$ at each time step.
4. The scheme is stable up to a Courant number of one and makes use of transverse Riemann solvers in order to avoid dimensional splitting.

The reader is directed to the paper of RBL [51] for a detailed explanation of all of the above points.

4.2. Passive tracer advection on the sphere

The first equation that we consider solving on the sphere is the advection equation. This PDE models the flow of a passive tracer along a prescribed velocity field. In generalized coordinates the advection equation can be written as

$$\frac{\partial}{\partial t}\left(\sqrt{G}q\right) + \sqrt{G}u^1\frac{\partial}{\partial x^1}q + \sqrt{G}u^2\frac{\partial}{\partial x^2}q = 0, \tag{12}$$

where $q(\vec{x},t)$ is the passive tracer concentration, $\vec{u}(\vec{x},t) = (u^1,u^2)$ is the velocity represented in the coordinate basis of (x^1,x^2). If the velocity is non-divergent, then

$$\sqrt{G}\vec{\nabla}\cdot\vec{u} = \frac{\partial}{\partial x^1}\left(\sqrt{G}u^1\right) + \frac{\partial}{\partial x^2}\left(\sqrt{G}u^2\right) = 0. \tag{13}$$

In this case, the passive tracer is conserved and one can define a streamfunction, ψ, such that

$$\sqrt{G}u^1 = \frac{\partial\psi}{\partial x^2} \quad \text{and} \quad \sqrt{G}u^2 = -\frac{\partial\psi}{\partial x^1}. \tag{14}$$

Before describing the numerical discretization, we note that although the focus of this section is on advection in a non-divergent velocity field, all the ideas presented here can readily be extended to the general case.

4.2.1. Numerical treatment

Because advection can be described entirely by two scalar functions, $q(\vec{x},t)$ and $\psi(\vec{x},t)$, the BLR wave propagation scheme for approximately solving this equation simplifies greatly. On the other hand, some heed must be paid to condition (13). The numerical strategy for this equation is described below.

Eq. (12) along with constraint (13) is equivalent to a conservation law for q, and therefore, a reasonable requirement for a numerical discretization of this system is that the overall update be conservative. If the equation is solved in advective form (12), then conservation is tantamount to requiring that the velocity on the numerical grid satisfies an appropriate discrete version of constraint (13). LeVeque [36] introduced a wave propagation algorithm with these properties, and in this section we will extend his method to advection on a general curved manifold $\mathscr{M}$.

The key to satisfying a discrete non-divergent condition is to introduce a staggered velocity field and streamfunction. Following LeVeque [36], we use the following grid staggering (see Fig. 5(a)):

$$\begin{aligned}
&\text{at Cell Centers :} && Q^n_{ij},\\
&\text{at Cell Corners :} && \psi^{n+1/2}_{i-1/2,j-1/2},\\
&\text{at Left/Right Edges :} && [u^1]^{n+1/2}_{i-1/2,j},\\
&\text{at Top/Bottom Edges :} && [u^2]^{n+1/2}_{i,j-1/2}.
\end{aligned}$$

We note that the streamfunction and velocity values are also staggered in time; this is necessary for full second-order accuracy if the velocity field is time dependent (see LeVeque [36]). Note that we can easily evaluate ψ at $t = t^{n+1/2}$, since we are assuming that this is a prescribed function. The velocity components u^1 and u^2 are obtained by differencing the streamfunction:

$$\left(\sqrt{G}u^1\right)^{n+1/2}_{i-1/2,j} = \frac{\psi^{n+1/2}_{i-1/2,j+1/2} - \psi^{n+1/2}_{i-1/2,j-1/2}}{\Delta x^2}, \tag{15}$$

$$\left(\sqrt{G}u^2\right)^{n+1/2}_{i,j-1/2} = \frac{\psi^{n+1/2}_{i-1/2,j-1/2} - \psi^{n+1/2}_{i+1/2,j-1/2}}{\Delta x^1}. \tag{16}$$

With these definitions, the following discrete divergence-free condition is satisfied in each grid cell:

$$\frac{(\sqrt{G}u^1)^{n+1/2}_{i+1/2,j} - \left(\sqrt{G}u^1\right)^{n+1/2}_{i-1/2,j}}{\Delta x^1} + \frac{\left(\sqrt{G}u^2\right)^{n+1/2}_{i,j+1/2} - \left(\sqrt{G}u^2\right)^{n+1/2}_{i,j-1/2}}{\Delta x^2} = 0. \tag{17}$$

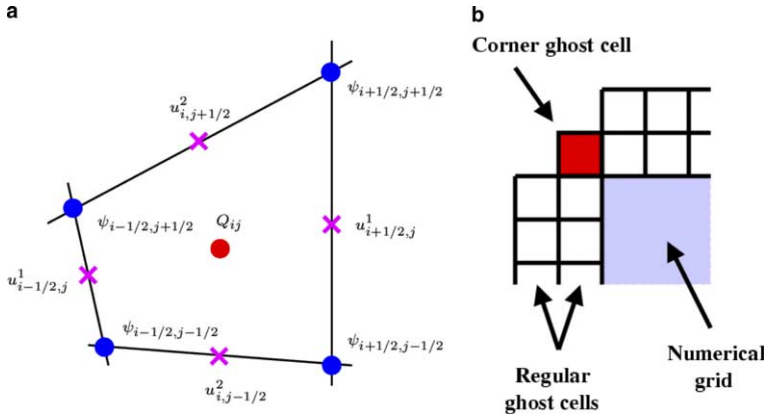

Fig. 5. (a) Grid staggering for advection on a logically Cartesian grid. The streamfunction (ψ) is placed at cell corners, the velocity components (u^1 and u^2), which are computed by differencing the streamfunction, are located at cell edges, and the concentration (Q) is located at cell centers. (b) Two layers of ghost cells are required in the wave propagation method in order to compute and limit the fluxes at grid boundaries. When transverse corrections are included the "corner ghost cells" also actively contribute to the solution on the interior.

Using the above definitions of the discrete velocity field, the fluctuations and second-order corrections that are required in update formula (8) take on the following form:

$$\mathscr{A}_1^{\pm}\Delta Q_{i-1/2,j} = \left[\left(\sqrt{G}u^1\right)^{n+1/2}_{i-1/2,j}\right]^{\pm}\left(Q^n_{ij} - Q^n_{i-1,j}\right),$$

$$\mathscr{A}_2^{\pm}\Delta Q_{i,j-1/2} = \left[\left(\sqrt{G}u^2\right)^{n+1/2}_{i,j-1/2}\right]^{\pm}\left(Q^n_{ij} - Q^n_{i,j-1}\right),$$

$$\widetilde{F}^1_{i-1/2,j} = \frac{1}{2}\left|\left(\sqrt{G}u^1\right)^{n+1/2}_{i-1/2,j}\right|\left(1 - \frac{\Delta t}{\Delta x^1}\left|\left(\sqrt{G}u^1\right)^{n+1/2}_{i-1/2,j}\right|\right)\left(Q^n_{ij} - Q^n_{i-1,j}\right)\phi(\theta_{i-1/2,j}),$$

$$\widetilde{F}^2_{i,j-1/2} = \frac{1}{2}\left|\left(\sqrt{G}u^2\right)^{n+1/2}_{i,j-1/2}\right|\left(1 - \frac{\Delta t}{\Delta x^2}\left|\left(\sqrt{G}u^2\right)^{n+1/2}_{i,j-1/2}\right|\right)\left(Q^n_{ij} - Q^n_{i,j-1}\right)\phi(\theta_{i,j-1/2}),$$

where $\phi(\theta)$ is a TVD (total variation diminishing) wave limiter function, θ is a measure of the local smoothness, and

$$[X]^+ \equiv \max(X,0) \quad \text{and} \quad [X]^- \equiv \min(X,0). \tag{18}$$

In this work, we make use the van Leer limiter function [60];

$$\phi(\theta) = \frac{\theta + |\theta|}{1 + |\theta|};$$

we refer the reader to LeVeque [39] and the references therein to a complete discussion of TVD wave limiters. In order to improve the accuracy and stability of this update, *transverse corrections*, which eliminate the need for dimensional splitting must also be incorporated into the $\widetilde{F}$'s (see [36,37,39]).

Under the assumption that the staggered velocities are computed from definitions (15) and (16), one can show that the wave propagation update described above is formally second-order accurate for smooth solutions, numerically conservative, and stable under the CFL condition

$$\max\left(|u^1|\frac{\Delta t}{\Delta x^1}, |u^2|\frac{\Delta t}{\Delta x^2}\right) < 1, \tag{19}$$

where $|u^1|$ and $|u^2|$ are the maximum velocity components on the computational grid at time level $t = t^{n+1/2}$ [36,39].

Finally, we note that a similar second-order method for advection was introduced by Hubbard and Nikiforakis [30]. Their method differs from the one presented here in that they solve Eq. (12) in flux form, use dimensional splitting, and solve on a longitude–latitude grid. Furthermore, Hubbard and Nikiforakis

considered advection in three-dimensions with adaptive mesh refinement (AMR), while we restrict ourselves to advection confined to the surface of the sphere and do not include AMR. Both of these extensions will be the focus of future work.

4.2.2. Boundary conditions

Because the advection of a passive tracer in an incompressible velocity field is described entirely by three scalar functions, q, ψ, and $\sqrt{G}$, boundary conditions between grid patches can be handled by directly copying these three functions at the appropriate spatial locations from one grid into the ghost cells of its neighbor. We note that the orientation from one grid patch to another may not be the same.

In order to obtain a stable and accurate wave propagation method, two layers of ghost cells are required. The inner layer is used to compute fluctuations and unlimited second-order corrections on the boundary, while the outer layer is used to limit the second-order corrections on the boundary. When the transverse corrections of LeVeque [36,37] are introduced, in addition to these two layers of ghost cells we also need ghost cells at grid patch corners (see Fig. 5(b)). These corner cells are needed because in a single time step normal Riemann problems cause the corners to influence adjacent ghost cells, but transverse Riemann solvers take these modifications into the physical domain. Note that with the direct copying strategy, the regular ghost cells from the left and right match up exactly with the regular ghost cells from the top and bottom (see Fig. 3(a)); in other words, the "corner ghost cells" have zero area. Because of this, information from the left layer of ghost cells, for example, can propagate directly into the top and bottom layers of ghost cells, which through the transverse corrections will then affect the solution in the interior. In practice we account for these corner contributions in the following way.

1. In the loop during which fluxes in the 1-direction are being computed (i.e., $\mathscr{A}_1^{\pm}\Delta Q$ and $\widetilde{F}^1$), we set:

$$Q_{0,0} = Q_{0,1} \text{ (Lower-left corner)},$$
$$Q_{0,m+1} = Q_{0,m} \text{ (Upper-left corner)},$$
$$Q_{m+1,0} = Q_{m+1,1} \text{ (Lower-right corner)},$$
$$Q_{m+1,m+1} = Q_{m+1,m} \text{ (Upper-right corner)}.$$

2. In the loop during which fluxes in the 2-direction are being computed (i.e., $\mathscr{A}_2^{\pm}\Delta Q$ and $\widetilde{F}^2$), we set:

$$Q_{0,0} = Q_{1,0} \text{ (Lower-left corner)},$$
$$Q_{0,m+1} = Q_{1,m+1} \text{ (Upper-left corner)},$$
$$Q_{m+1,0} = Q_{m,0} \text{ (Lower-right corner)},$$
$$Q_{m+1,m+1} = Q_{m,m+1} \text{ (Upper-right corner)},$$

where m is the number of points in either direction in the interior of the grid. In words, the above procedure says that the solution values in the computational corner cells are set to the solution values in one of the two cells immediately next to it; which cell is chosen depends on whether a 1-sweep or a 2-sweep is being carried out. A similar procedure also has to be applied to the square root of the determinant of the metric, $\sqrt{G}$, and the streamfunction, ψ. This approach guarantees that the overall method is globally conservative and stable under CFL condition (19).

4.3. Shallow water flow on the sphere

The shallow water equations were first introduced by Saint-Venant as a model for river flow [13]. These equations can be derived from the Navier–Stokes equations by assuming that the fluid is inviscid, hydrostatically balanced in the vertical direction, and of constant density [46]. Although the constant density assumption is not realistic for large-scale oceanic and atmospheric flows, these equations are often used as a test problem for global circulation codes [61]. In generalized coordinates the shallow water system can be written as

$$\frac{\partial}{\partial t}\begin{bmatrix} h \\ hu^1 \\ hu^2 \end{bmatrix} + \frac{1}{\sqrt{G}}\frac{\partial}{\partial x^k}\left(\sqrt{G}\begin{bmatrix} hu^k \\ \mathscr{T}^{1k} \\ \mathscr{T}^{2k} \end{bmatrix}\right) = \Psi_C + \Psi_B + \begin{bmatrix} 0 \\ -\Gamma^1_{ij}\mathscr{T}^{ji} \\ -\Gamma^2_{ij}\mathscr{T}^{ji} \end{bmatrix}, \tag{20}$$

where h is the thickness of the shallow water layer, $\vec{u} = (u^1, u^2)$ is the fluid velocity, g is the gravitational constant, and $\vec{\Psi}_C$ and $\vec{\Psi}_B$ are the source terms due to the Coriolis force and variable bottom topography, respectively. The components of the momentum tensor are

$$\mathscr{T}^{ij} = hu^i u^j + \frac{1}{2}gh^2 G^{ij}. \tag{21}$$

In component form, the Coriolis source term can be written as

$$\Psi_C = \frac{f}{\sqrt{G}}\begin{bmatrix} 0 \\ G_{12}hu^1 + G_{22}hu^2 \\ -G_{11}hu^1 - G_{12}hu^2 \end{bmatrix}, \tag{22}$$

where $f = 2\Omega\sin(\theta)$ is Coriolis parameter and Ω is the Earth's angular velocity. The source term due to a variable bottom topography can be written in component form as follows:

$$\Psi_B = \Psi_{B,1} + \Psi_{B,2} = -gh\begin{bmatrix} 0 \\ G^{11}\frac{\partial b}{\partial x^1} \\ G^{12}\frac{\partial b}{\partial x^1} \end{bmatrix} - gh\begin{bmatrix} 0 \\ G^{12}\frac{\partial b}{\partial x^2} \\ G^{22}\frac{\partial b}{\partial x^2} \end{bmatrix}, \tag{23}$$

where $b = b(\lambda, \theta)$ describes the bottom topography (i.e., mountains). The reason that Ψ_B is split into $\Psi_{B,1}$ and $\Psi_{B,2}$ is explained below in the section on *numerical treatment*.

4.3.1. Numerical treatment

The curved manifold wave propagation method described in Section 4.1 updates the solution by solving orthonormal Riemann problems; the orthonormal form of the shallow water equations are

$$\frac{\partial}{\partial t}\begin{bmatrix} h \\ hu^{\hat{1}} \\ hu^{\hat{2}} \end{bmatrix} + \frac{\partial}{\partial x^{\hat{k}}}\begin{bmatrix} hu^{\hat{k}} \\ hu^{\hat{1}}u^{\hat{k}} + \frac{1}{2}gh^2\delta^{1\hat{k}} \\ hu^{\hat{2}}u^{\hat{k}} + \frac{1}{2}gh^2\delta^{2\hat{k}} \end{bmatrix} = 0, \tag{24}$$

where we have momentarily ignored the Coriolis and the topographic source terms, $u^{\hat{k}}$ denotes the kth component of $\vec{u}$ after orthonormalization, and δ^{ij} is the Cartesian metric:

$$\delta^{ij} = \begin{cases} 1 & \text{if } i = j, \\ 0, & \text{otherwise.} \end{cases}$$

The eigenvalues of the linearized flux Jacobian in the $\hat{1}$-direction are given by:

$$\lambda_{1,3} = \bar{u}^{\hat{1}} \pm \sqrt{g\bar{h}} \text{ (Gravity waves)},$$
$$\lambda_2 = \bar{u}^{\hat{1}} \text{ (Rossby wave)},$$

where the Roe averages are (see pp. 320–322 of LeVeque [39] for a detailed derivation)

$$\bar{h} \equiv \frac{1}{2}(h_{\mathrm{l}} + h_{\mathrm{r}}), \quad \bar{u}^{\hat{1},\hat{2}} \equiv \frac{\sqrt{h_{\mathrm{l}}}u_{\mathrm{l}}^{\hat{1},\hat{2}} + \sqrt{h_{\mathrm{r}}}u_{\mathrm{r}}^{\hat{1},\hat{2}}}{\sqrt{h_{\mathrm{l}}} + \sqrt{h_{\mathrm{r}}}}.$$

The eigenvectors of the linearized flux Jacobian can also be readily computed, and are given, for example, on p. 481 of LeVeque [39]. Note that geometric scalings in the eigenvalues and eigenvectors are accounted for through the de-orthonormalization procedure that must be applied in the RBL wave propagation method.

As described in Section 4.1, the action of parallel transport provides a mechanism for discretizing the geometric source term. The Coriolis force term, on the other hand, is handled by using Strang operator splitting to split the Coriolis term from the rest of Eq. (20). The operator splitting approach leads to the following Coriolis force ODE that must be solved twice in each time step [39]:

$$\frac{\partial}{\partial t}\begin{bmatrix} hu^1 \\ hu^2 \end{bmatrix} = \frac{f}{\sqrt{G}}\begin{bmatrix} G_{12}hu^1 + G_{22}hu^2 \\ -G_{11}hu^1 - G_{12}hu^2 \end{bmatrix}.$$

We solve this linear ODE exactly. Finally, the topographic source term is handled by splitting Ψ_B into $\Psi_{B,1}$ and $\Psi_{B,2}$ (see above), and then incorporating these two pieces into normal Riemann problems using the strategy of Bale et al. [3]; $\Psi_{B,1}$ is incorporated into the 1-direction Riemann problems and $\Psi_{B,2}$ into the 2-direction Riemann problems.

4.3.2. Boundary conditions

The boundary conditions for hyperbolic systems are applied using Method 2 as described in Section 3.2. One-dimensional linear interpolation along great circles is required in order to get information from neighboring grids into the ghost cells of the current grid. Two layers of ghost cells are used; the inner layer is required for computing fluxes, while the outer layer is used to limit these fluxes. Unlike Method 1, Method 2 for the boundary conditions does not require any special treatment of the corner ghost cell. We note that this procedure does not in general guarantee (mass) conservation across internal boundaries. Simple fixes can be implemented to overcome this loss of conservation, but we have found that such procedures can generate noise at the internal boundaries. We will show in this section that the loss of conservation neither degrades the accuracy of the overall method, nor does it affect the shock-capturing ability of the method.

4.4. Shallow water MHD on the non-rotating sphere

The shallow water magnetohydrodynamic (SMHD) equations were introduced by Gilman [20] as a model for the solar tachocline. This system is a simplification of the ideal magnetohydrodynamic (MHD) equations and describes the dynamics of a thin, constant density, quasi-neutral plasma layer that is hydrostatically balanced in the radial direction. SMHD is the ideal MHD analog of the shallow water equations. In generalized coordinates the system can be written as

$$\frac{\partial}{\partial t}\begin{bmatrix} h \\ hu^1 \\ hu^2 \\ hB^1 \\ hB^2 \end{bmatrix} + \frac{1}{\sqrt{G}}\frac{\partial}{\partial x^k}\left(\sqrt{G}\begin{bmatrix} hu^k \\ \mathscr{T}^{1k} \\ \mathscr{T}^{2k} \\ hu^kB^1 - hu^1B^k \\ hu^kB^2 - hu^2B^k \end{bmatrix}\right) = \begin{bmatrix} 0 \\ -\Gamma^1_{ij}\mathscr{T}^{ji} \\ -\Gamma^2_{ij}\mathscr{T}^{ji} \\ 0 \\ 0 \end{bmatrix}, \tag{25}$$

where h is the thickness of the plasma layer, $\vec{u} = (u^1, u^2)$ is the fluid velocity, $\vec{B} = (B^1, B^2)$ is the magnetic field, and g is the gravitational constant. The components of the momentum tensor are

$$\mathscr{T}^{ij} = hu^iu^j - hB^iB^j + \frac{1}{2}gh^2G^{ij}. \tag{26}$$

Note that for system (25) a geometric source term appears only in the momentum equation; this is due to the fact that the magnetic field tensor has zeros along the diagonal and is anti-symmetric:

$$\mathscr{B}^{ij} \equiv hu^iB^j - hu^jB^i \Rightarrow \mathscr{B}^{ii} = 0 \quad \text{and} \quad \mathscr{B}^{ij} = -\mathscr{B}^{ji}.$$

4.4.1. Numerical treatment

The orthonormal form of the SMHD equations are

$$\frac{\partial}{\partial t}\begin{bmatrix} h \\ hu^{\hat{1}} \\ hu^{\hat{2}} \\ hB^{\hat{1}} \\ hB^{\hat{2}} \end{bmatrix} + \frac{\partial}{\partial x^{\hat{k}}}\begin{bmatrix} hu^{\hat{k}} \\ hu^{\hat{1}}u^{\hat{k}} - hB^{\hat{1}}B^{\hat{k}} + \frac{1}{2}gh^2\delta^{1\hat{k}} \\ hu^{\hat{2}}u^{\hat{k}} - hB^{\hat{2}}B^{\hat{k}} + \frac{1}{2}gh^2\delta^{2\hat{k}} \\ hu^{\hat{k}}B^{\hat{1}} - hu^{\hat{1}}B^{\hat{k}} \\ hu^{\hat{k}}B^{\hat{2}} - hu^{\hat{2}}B^{\hat{k}} \end{bmatrix} = 0, \tag{27}$$

where $u^{\hat{k}}$ denotes the kth component of $\vec{u}$ after orthonormalization and δ^{ij} is the Cartesian metric. The eigenvalues of the linearized flux Jacobian in the $\hat{1}$-direction are given by:

$$\lambda_{1,5} = \bar{u}^{\hat{1}} \pm \sqrt{(\bar{B}^{\hat{1}})^2 + g\bar{h}} \text{ (Magnetogravity waves)},$$
$$\lambda_{2,4} = \bar{u}^{\hat{1}} \pm \bar{B}^{\hat{1}} \text{ (Alfvén waves)},$$
$$\lambda_{3} = \bar{u}^{\hat{1}} \text{ (Divergence wave)},$$

where the Roe averages are (see the appendix of De Sterck [54] for a detailed derivation)

$$\bar{h} \equiv \frac{1}{2}(h_{\mathrm{l}} + h_{\mathrm{r}}), \quad \bar{u}^{\hat{1},\hat{2}} \equiv \frac{\sqrt{h_{\mathrm{l}}}u_{\mathrm{l}}^{\hat{1},\hat{2}} + \sqrt{h_{\mathrm{r}}}u_{\mathrm{r}}^{\hat{1},\hat{2}}}{\sqrt{h_{\mathrm{l}}} + \sqrt{h_{\mathrm{r}}}}, \quad \bar{B}^{\hat{1},\hat{2}} \equiv \frac{\sqrt{h_{\mathrm{l}}}B_{\mathrm{l}}^{\hat{1},\hat{2}} + \sqrt{h_{\mathrm{r}}}B_{\mathrm{r}}^{\hat{1},\hat{2}}}{\sqrt{h_{\mathrm{l}}} + \sqrt{h_{\mathrm{r}}}}.$$

The eigenvectors of the linearized flux Jacobian can also be readily computed, and are given, for example, in the Appendix of De Sterck [54]. Note that geometric scalings in the eigenvalues and eigenvectors are accounted for through the de-orthonormalization procedure that must be applied in the RBL wave propagation method.

4.4.2. Divergence-free constraint

In addition to system (25), the magnetic field must satisfy a divergence-free condition as required by Maxwell's equations; this constraint comes about because magnetic monopoles have never been found either in nature or in the laboratory [32]. For the shallow water MHD equations the correct divergence-free condition can be obtained by depth-averaging the usual divergence-free constraint from Maxwell's equations and applying the appropriate boundary conditions at $z = 0$ and $z = h$ [54]. The result of this process is the following constraint:

$$\sqrt{G}\vec{\nabla}\cdot(h\vec{B}) = \frac{\partial}{\partial x^1}\left(\sqrt{G}hB^1\right) + \frac{\partial}{\partial x^2}\left(\sqrt{G}hB^2\right) = 0, \tag{28}$$

which must be satisfied for all space and time.

It can be easily shown that any exact solution of the original SMHD system (25) will automatically satisfy constraint (28) provided that the initial condition also satisfies (28) (see for example Tóth [55]). Numerical solutions to SMHD, however, are not exact, and in general only satisfy the divergence-free constraint to the truncation error of the numerical scheme. Brackbill and Barnes [10] showed that this numerical error can lead to inaccuracies in the momentum flux, which can strongly contaminate the overall solution; this observation has been confirmed in many subsequent papers. A variety of numerical approaches have been introduced in order to avoid this problem; see Tóth [55] and references therein for a review of these methods.

In this work we make use of the constrained transport of [50], which was originally designed for ideal MHD. This method is referred to as the MPACT scheme (magnetic potential advection constrained transport), and is an unstaggered variant of the original constrained transport method developed by Evans and Hawley [14]. MPACT is built on first introducing a magnetic potential, $\mathbb{A}$, which is related to the magnetic field in the following way:

$$h\vec{B} = \nabla \times (0, 0, \mathbb{A})^{\mathrm{T}} = \frac{1}{\sqrt{G}}\begin{bmatrix} \frac{\partial \mathbb{A}}{\partial x^2} \\ -\frac{\partial \mathbb{A}}{\partial x^1} \end{bmatrix}. \tag{29}$$

Note that only the radial component of the magnetic potential is dynamically important. Rewriting the evolution equation for the magnetic field in terms of the magnetic potential produces the following scalar equation:

$$\frac{\partial \mathbb{A}}{\partial t} + \Omega = 0, \tag{30}$$

where Ω is the radial component of the electric field and satisfies Ohm's law [32];

$$\Omega = (h\vec{B} \times \vec{u}) \cdot \hat{r} = \sqrt{G}(hB^1u^2 - hB^2u^1). \tag{31}$$

Combining (29)–(31) gives the following magnetic potential advection equation:

$$\frac{\partial \mathbb{A}}{\partial t} + u^1 \frac{\partial \mathbb{A}}{\partial x^1} + u^2 \frac{\partial \mathbb{A}}{\partial x^2} = 0. \tag{32}$$

This equation is linear, scalar, and hyperbolic, but in general it is not a conservation law. Although Eq. (32) can be made into a conservation law for the quantity $\sqrt{G}h\mathbb{A}$, we opt for the non-conservative formulation because $\mathbb{A}$ is guaranteed to be continuous, while $\sqrt{G}h\mathbb{A}$ may be discontinuous.

The idea behind the MPACT scheme is to solve Eq. (32) directly and obtain a divergence-free magnetic field by finite differencing the resulting magnetic potential. A key ingredient is the use of specially designed limiters that produce a non-oscillatory magnetic field during the time update for the magnetic potential. We omit the details of the limiting procedure here, and instead refer the reader to [50]. A single time step in the MPACT scheme can be broken down into the following four steps [50]:

Step 1. Solve SMHD system (25): $(h^n, h\vec{u}^n, h\vec{B}^n) \to (h^{n+1}, h\vec{u}^{n+1}, h\vec{B}^{\star})$; (*Note:* the quantity $h\vec{B}^{\star}$ is not divergence-free and is discarded.)
Step 2. Time average the velocity field: $\vec{u}^{n+1/2} = \frac{1}{2}(\vec{u}^n + \vec{u}^{n+1})$.
Step 3. Solve magnetic potential equation (32) with $\vec{u}^{n+1/2}$: $\mathbb{A}^n \to \mathbb{A}^{n+1}$.
Step 4. Update the magnetic field:

$$[hB_1]_{ij}^{n+1} = \frac{\mathbb{A}_{i,j+1}^{n+1} - \mathbb{A}_{i,j-1}^{n+1}}{2\sqrt{G_{ij}}\Delta x^2} \quad \text{and} \quad [hB_2]_{ij}^{n+1} = \frac{\mathbb{A}_{i-1,j}^{n+1} - \mathbb{A}_{i+1,j}^{n+1}}{2\sqrt{G_{ij}}\Delta x^1}.$$

This approach guarantees that the following discrete divergence is identically zero:

$$\sqrt{G_{ij}}[\vec{\nabla} \cdot (h\vec{B})]_{ij}^{n+1} \equiv \frac{\sqrt{G_{i+1,j}}[hB_1]_{i+1,j}^{n+1} - \sqrt{G_{i-1,j}}[hB_1]_{i-1,j}^{n+1}}{2\Delta x^1} + \frac{\sqrt{G_{i,j+1}}[hB_2]_{i,j+1}^{n+1} - \sqrt{G_{i,j-1}}[hB_2]_{i,j-1}^{n+1}}{2\Delta x^2} = 0.$$

We note that in this method there is no grid staggering and the only averaging required in the numerical update is the temporal averaging in Step 2. Details on how Step 3 is carried out can be found in [50]. In [50] this method is shown to produce second-order accuracy for smooth solutions (in all the computed variables, in both space and time) and non-oscillatory solutions near shock waves. Although the results of [50] focused only on the ideal MHD equations on Cartesian grids, we demonstrate in this work that the MPACT also works well for the SMHD equations on the sphere.

4.4.3. Boundary conditions

For the SMHD equations, we again make use of the interpolation approach of Method 2 (see Section 3.2), which was also used for the shallow water equations (see Section 4.3). However, there are two main differences between the shallow water and the SMHD implementation of the boundary conditions. First, the MPACT scheme as described above requires three different applications of the boundary conditions during one time step:

1. BCs on $(h, h\vec{u}, h\vec{B})^n$ then Step 1,
2. BCs on $\vec{u}^{n+1}$ then Step 2 and Step 3,
3. BCs on $\mathbb{A}^{n+1}$ then Step 4.

Second, in order to get an accurate representation of the magnetic field, we require that all the magnetic potential values that are used in Step 4 have been updated with limited second-order corrections in Step 3. This can only be achieved if a third layer of ghost cells is added to each of the six cubed sphere grids, since

we need the magnetic potential in the first layer of ghost cells. We note that these additional considerations add very little to the overall cost of the method, since boundary conditions require only $\mathcal{O}(N)$ operations on an $N \times N \times 6$ grid.

5. Numerical examples

In this section, the proposed numerical method is validated on several test problems for the advection, shallow water, and SMHD equations. Relative errors in these test problems are measured using the following definitions:

$$L_1 \equiv \frac{I\left(|Q_{ij}^n - X_{ij}^n|\right)}{I\left(|X_{ij}^n|\right)}, \quad L_2 \equiv \sqrt{\frac{I\left((Q_{ij}^n - X_{ij}^n)^2\right)}{I\left(\left(X_{ij}^n\right)^2\right)}}, \quad L_\infty \equiv \frac{\max\limits_{i,j,m} |Q_{ij}^n - X_{ij}^n|}{\max\limits_{i,j,m} |X_{ij}^n|},$$

where Q is the numerical approximation, X is the exact solution sampled on the numerical grid, and

$$I(Q) \equiv \sum_{m=1}^{6} \sum_{i=1}^{N} \sum_{j=1}^{N} \left[Q_{ij}^n \sqrt{G_{ij}} \right]_m, \tag{33}$$

where m is the grid patch index.

5.1. Advection of a cosine bell

We first consider the solid rotation test case suggested by Williamson et al. [61] (Problem #1). For this problem, the streamfunction is set for solid body rotation around the sphere at an angle of α with respect to the equatorial plane;

$$\psi(\lambda, \theta; \alpha) = 2\pi(\cos(\alpha)\sin(\theta) - \sin(\alpha)\cos\left(\lambda - \frac{\pi}{4}\right)\cos(\theta)), \tag{34}$$

where coordinate components of the velocity are computed through Eqs. (15) and (16). Note that our definitions of u^λ differs from the definition of the same quantity in Williamson et al. [61] by a factor of $\cos(\theta)$; this is due to the fact that we are taking our velocity components to be components in a *coordinate basis*. The magnitude of the velocity field has been chosen so that after one unit of time, the initial condition has made one full revolution around the unit sphere. The initial concentration in spherical coordinates is given by:

$$q(\lambda, \theta) = \begin{cases} 0.5(1 + \cos(3\pi s)) & \text{if } s < 1/3, \\ 0, & \text{otherwise,} \end{cases}$$

where $s = \text{dist}(\lambda, \theta, -\pi/4, 0)$, meaning that the initial condition is centered at the point $(\lambda, \theta) = (-\pi/4, 0)$ on the equator. Since the exact solution to this problem is smooth, we will use it to verify the order of accuracy of the method.

The results of numerical convergence studies for $\alpha = 90°$ (advection over the poles) and $\alpha = 45°$ (advection through the corners) are shown in Tables 2 and 3, respectively. Second-order accuracy in the relative L_1, L_2, and L_∞ norms is evident for both examples. Shown in Fig. 6 are contour plots of the solution with four different grid resolutions for the $\alpha = 45°$ example. Shown in each plot are equally spaced contour lines from $q = 0$ to $q = 0.9$; dashed lines represent the initial condition and solid lines represent the solution at $t = 5$. These plots show that even after five full trips around the sphere, through four of the eight corner points on each trip, and along two interfaces on each trip, the solution remains accurate. No spurious oscillations are present and no noise is generated from the corners or internal boundaries.

5.2. Advection of a discontinuous pattern

Next we consider the problem of advecting a discontinuous profile. The initial condition for this problem is the following "target" profile:

Table 2
Convergence study for Williamson et al. [61] Test Case 1 – advection of a cosine bell

Grid	Error at $t = 1$			Error at $t = 5$		
	L_1	L_2	L_∞	L_1	L_2	L_∞
20	2.48e − 1	1.96e − 1	1.83e − 1	6.68e − 1	4.81e − 1	4.87e − 1
40	5.70e − 2	4.62e − 2	4.57e − 2	1.97e − 1	1.54e − 1	1.41e − 1
80	1.47e − 2	1.20e − 2	1.48e − 2	5.60e − 2	4.51e − 2	4.00e − 2
160	3.77e − 3	3.22e − 3	6.26e − 3	1.61e − 2	1.28e − 2	1.51e − 2
Order	2.01	1.97	1.62	1.80	1.75	1.69

Shown are the relative errors after one and five revolutions with solid body rotation at an angle of $\alpha = 90°$ to the equator. The orders of accuracy are obtained from a least squares fit through the data.

Table 3
Convergence study for Williamson et al. [61] Test Case 1 – advection of a cosine bell

Grid	Error at $t = 1$			Error at $t = 5$		
	L_1	L_2	L_∞	L_1	L_2	L_∞
20	5.02e − 1	4.01e − 1	4.62e − 1	1.01e + 0	6.87e − 1	7.26e − 1
40	1.12e − 1	1.07e − 1	1.76e − 1	3.99e − 1	3.31e − 1	4.13e − 1
80	2.12e − 2	2.23e − 2	5.85e − 2	8.37e − 2	7.74e − 2	1.36e − 1
160	4.77e − 3	5.32e − 3	1.96e − 2	1.72e − 2	1.67e − 2	4.19e − 2
Order	2.28	2.16	1.58	2.27	2.25	1.65

Shown are the relative errors after one and five revolutions with solid body rotation at an angle of $\alpha = 45°$ to the equator. The orders of accuracy are obtained from a least squares fit through the data. In this table, the $N = 20$ errors have been excluded in calculating the orders of accuracy.

$$q(\lambda,\theta) = \begin{cases} 1 & \text{if } \operatorname{dist}(\lambda,\theta,-\pi/4,0) < 0.4, \\ 1 & \text{if } 0.72 < \operatorname{dist}(\lambda,\theta,-\pi/4,0) < 1.12, \\ 0, & \text{otherwise,} \end{cases}$$

which is again centered on the point $(\lambda,\theta) = (-\pi/4,0)$ on the equator. The velocity field is again set to solid body rotation; for this problem we choose $\alpha = 0$ for rotation parallel to the equator. Note that choosing $\alpha = 90°$ would produce the same results. This initial condition is chosen so that the inner "circle" does not interact with the corner points, but the outer "ring" does. The gap between the circle and the ring will give an indication of how much numerical diffusion is introduced by the method. The solution on an $80 \times 80 \times 6$ grid is shown in Fig. 7 at time $t = 0$ and $t = 5$ (after five full rotations). In particular, displayed are pseudo-color plots of the solution (Fig. 7(a) and (c)), as well radial scatter plots of all the data points as measured from the center of the target pattern (Fig. 7(b) and (d)). These plots show that the proposed method accurately maintains the profile after five revolutions.

5.3. Steady-state geostrophic flow

For the first shallow water test problem, we consider the steady-state geostrophic flow problem of Williamson et al. [61] (Problem #2). For this example, we take the characteristic time scale to be one day (86,400 s), and the characteristic length scale to be the radius of the Earth (6,371,220 m). The non-dimensional gravitational constant and rotational rate take on the following values:

$$g = \left(9.80616\ \text{m s}^{-2}\right)\frac{(86,400\ \text{s})^2}{(6,371,220\ \text{m})} \approx 11,489.57,$$

$$\Omega = (86,400\ \text{s})(7.292 \times 10^{-5}\ \text{s}^{-1}) \approx 6.300288.$$

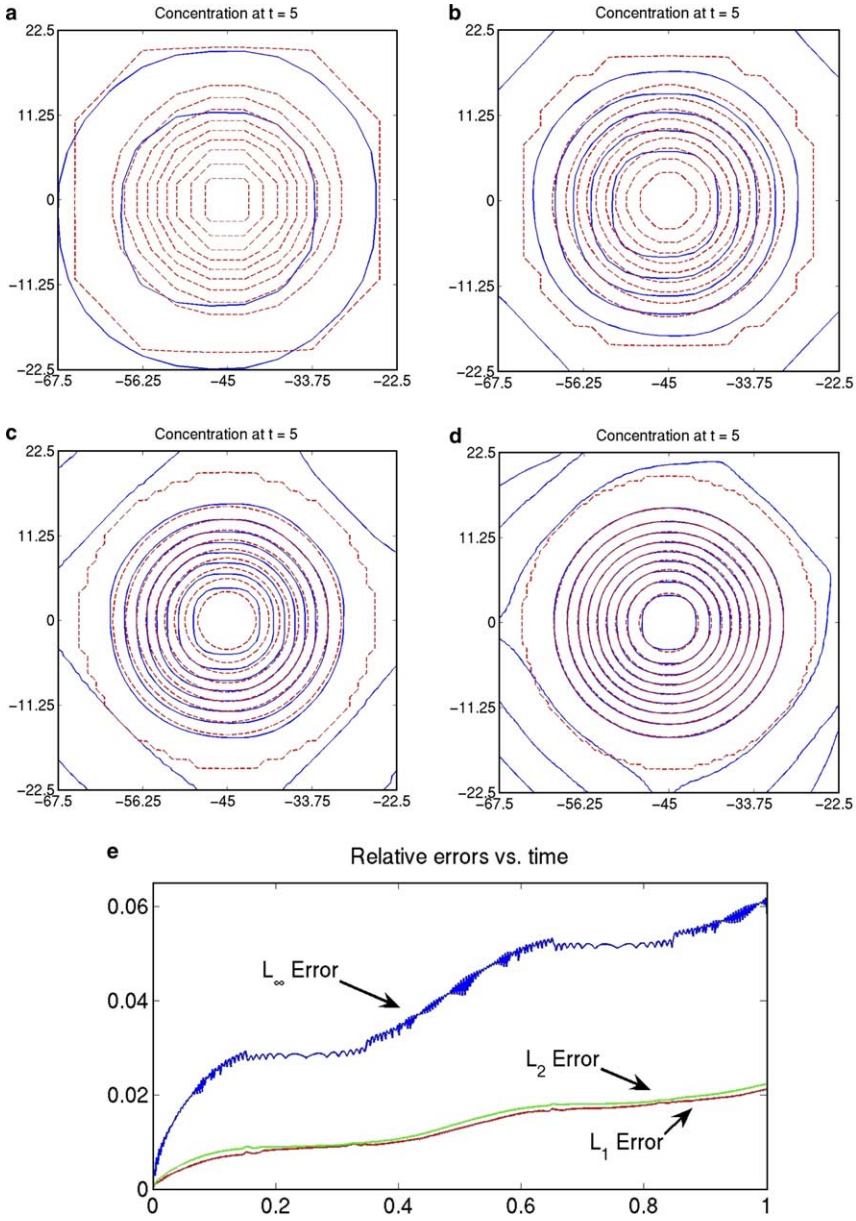

Fig. 6. Williamson et al. [61] Test Case 1 – advection of a cosine bell with $\alpha = 45°$. Shown in these plots are 10 equally spaced contours of concentration from 0 to 0.9 of the initial profile (dashed lines) as well as the solution after five full revolutions (solid lines). The different grid resolutions shown are (a) $20 \times 20 \times 6$, (b) $40 \times 40 \times 6$, (c) $80 \times 80 \times 6$, and (d) $160 \times 160 \times 6$. Shown in panel (e) is a plot of the relative L_1, L_2, and L_∞ errors as a function of time for the first revolution. The x and y axes in all of these plots are the longitude and latitude, respectively.

Unless otherwise noted, we will continue to use these non-dimensional parameters for the remainder of the shallow water examples.

In this test problem, the axis of rotation is tilted relative to the vertical axis by an angle α; this yields the following Coriolis parameter:

$$f = 2\Omega(\sin\theta\cos\alpha - \cos\theta\cos\lambda\sin\alpha).$$

The initial condition for this problem is the geostrophic solution, which is an exact balance between the pressure gradient and the Coriolis force [46]. The non-dimensional height and coordinate velocities for this solution can be written as follows:

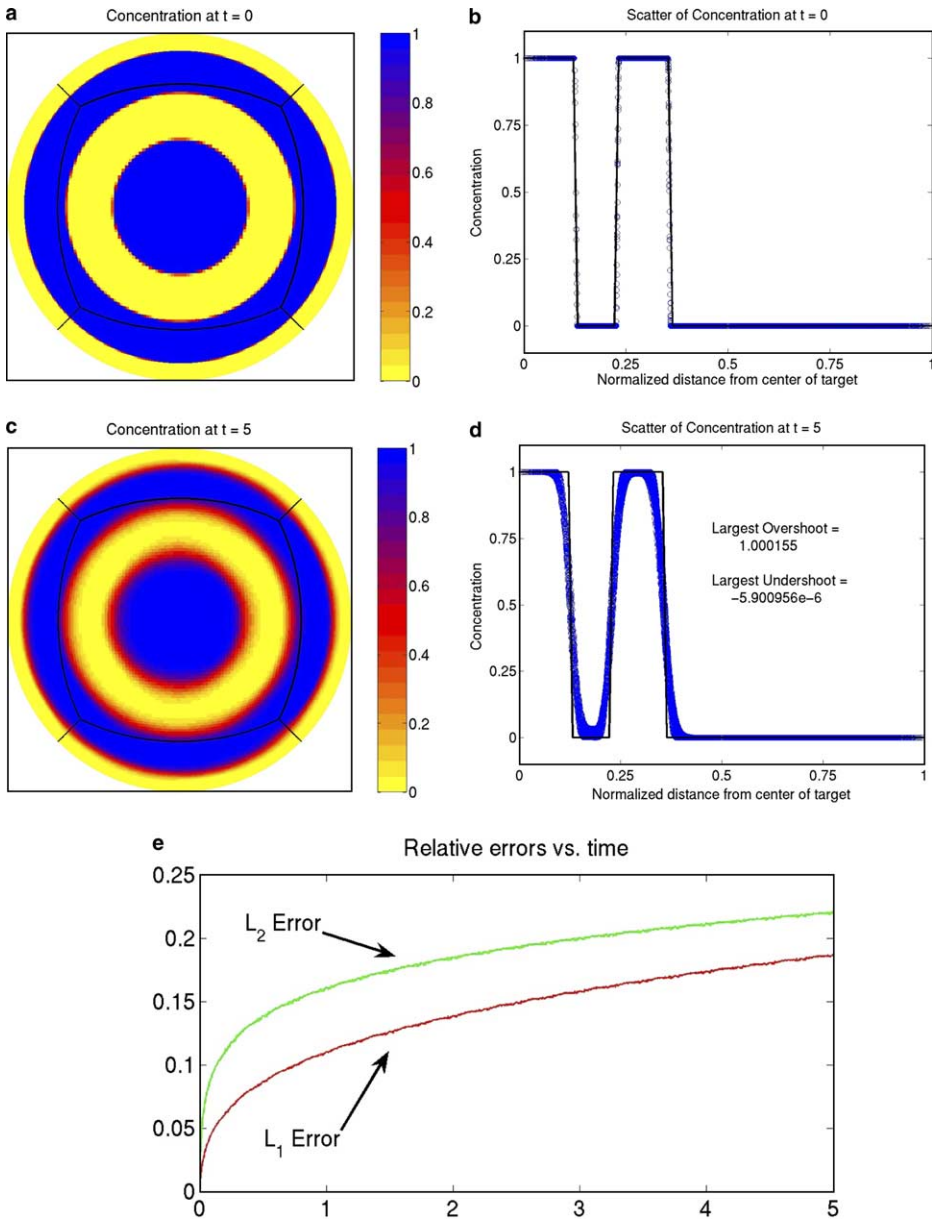

Fig. 7. Advection of a discontinuous profile along the equator with a grid resolution of $80 \times 80 \times 6$. Shown in these plots are (a) the initial concentration profile on the sphere, (b) a scatter plot of the initial profile, (c) the profile after 5 full revolutions on the sphere, (d) a scatter plot of the profile after 5 full revolutions, and (e) a plot of the relative L_1 and L_2 errors as a function of time. The black lines in plots (a) and (c) denote internal boundaries of the cubed sphere grid.

$$h = h_0 - \left(\frac{\Omega u_0}{g} + \frac{u_0^2}{2g}\right)\left(\frac{f}{2\Omega}\right)^2,$$
$$u^\lambda = u_0(\cos\alpha + \cos\lambda\tan\theta\sin\alpha),$$
$$u^\theta = -u_0\sin\lambda\sin\alpha,$$

where $h_0 = 4.7057 \times 10^{-4}$ and $u_0 = \pi/6$ (1 full rotation after 12 days). Note that our definitions of u^λ differs from the definition of the same quantity in Williamson et al. [61] by a factor of $\cos(\theta)$; this is due to the fact

that we are taking our velocity components to be components in a *coordinate basis*. The goal of this test case is to determine how accurately the geostrophic steady-state is maintained.

In Table 4, we show the results of the proposed method in the case where $\alpha = 45°$. In this example, the method is run out to five days ($t = 5$) using four different grid resolutions: $N \times N \times 6$, where $N = 20$, 40, 80, 160. The relative L_1, L_2, and L_∞ norm errors are shown in these tables and second-order accuracy is evident in all three norms.

Before moving on to the next example, we would like to point out the contrast between the current results and the convergence studies of Blikberg [8]. Blikberg made use of variant of the wave propagation method presented in this work in conjunction with a standard longitude–latitude grid. On this grid significant noise was generated near the poles, and subsequently no convergence was seen in the ∞-norm. Blikberg went on to speculate that the wave propagation method applied on a more evenly spaced grid would produce more accurate results; the results of the current study confirm this observation.

5.4. Steady-state geostrophic flow with compact support

Problem #3 from Williamson et al. [61] again involves simulating a geostrophically balanced flow, but this time with a height field that has compact support.

The initial height and coordinate velocities are as follows:

$$h = h_0 - \frac{1}{g}\int_{-\pi/2}^{\theta'} (2\Omega \sin(\tau)\mu(\tau) + \mu^2(\tau)\tan(\tau))\,\mathrm{d}\tau,$$

$$(u^1, u^2) = \left(\frac{1}{\sqrt{G}}\frac{\partial \psi}{\partial x^2}, -\frac{1}{\sqrt{G}}\frac{\partial \psi}{\partial x^1}\right),$$

where $h_0 = 4.7057 \times 10^{-4}$. In the numerical code, the above integrals and derivatives are computed to high accuracy using Gaussian quadrature and fourth-order finite difference operators. The expressions for $\mu(\theta)$ and $\psi(\lambda, \theta)$ can be obtained from the description of Test Case #3 in Williamson et al. [61]. A convergence study is presented in Table 5 with $\alpha = 60°$. The convergence rates in the L_2 and L_∞ norms are slightly lower than

Table 4
Convergence study for Williamson et al. [61] Test Case 2 – steady-state geostrophic flow

Grid	L_1 error	L_2 error	L_∞ error
20	4.99e − 3	5.37e − 3	8.80e − 3
40	9.96e − 4	1.11e − 3	2.65e − 3
80	2.22e − 4	2.52e − 4	6.95e − 4
160	5.22e − 5	6.02e − 5	2.13e − 4
Order	2.19	2.16	1.80

All of the errors listed here are relative errors in h and are computed at time $t = 5$ with $\alpha = 45°$. The orders of accuracy are obtained from a least squares fit through the data.

Table 5
Convergence study for Williamson et al. [61] Test Case 3 – steady-state geostrophic flow with compact support

Grid	L_1 error	L_2 error	L_∞ error
20	3.53e − 3	4.96e − 3	2.39e − 2
40	7.64e − 4	1.13e − 3	8.78e − 3
80	1.72e − 4	2.77e − 4	3.17e − 3
160	6.43e − 5	1.86e − 4	2.92e − 3
Order	1.95	1.62	1.02

All of the errors listed here are relative errors in h and are computed at time $t = 5$ with $\alpha = 60°$. The orders of accuracy are obtained from a least squares fit through the data.

those found in the previous example (Williamson et al. Problem #2). We have found that most of the error occurs in regions where the velocity magnitude should be analytically zero and the height should be constant; since the geostrophic balance is not exactly preserved by the numerical scheme, spurious flow is generated in these regions. Despite this fact, the errors in all norms are comparable to the errors found in the previous test case and the convergence rates in the L_1 and L_2 norms are essentially second order.

5.5. Forced non-linear system with a translating low

Problem #4 from Williamson et al. [61] involves simulating the advection of a localized disturbance on top of on a horizontal jet stream. The flow is known analytically; however, it is not a solution to the shallow water equations. Therefore, an additional forcing is applied to the shallow water equations so that the prescribed flow is an exact solution. If we define the following quantity:

$$\mathrm{SW}(h,u^1,u^2) \equiv \frac{\partial}{\partial t}\left(\sqrt{G}\begin{bmatrix} h \\ hu^1 \\ hu^2 \end{bmatrix}\right) + \frac{\partial}{\partial x^k}\left(\sqrt{G}\begin{bmatrix} hu^k \\ hu^1u^k + \frac{1}{2}gh^2G^{1k} \\ hu^2u^k + \frac{1}{2}gh^2G^{2k} \end{bmatrix}\right),$$

then in this test case we are faced with solving the following equation:

$$\mathrm{SW}(h,u^1,u^2) = \mathrm{SW}(\tilde{h},\tilde{u}^1,\tilde{u}^2),$$

where $(\tilde{h},\tilde{u}^1,\tilde{u}^2)$ is the prescribed flow. Note that we have analytically removed the Coriolis and geometric source terms in order to simplify the algebra; since these terms only depend on the undifferentiated solution, this will not significantly change the results of this test problem.

Numerically, the right-hand side of the above equation is handled by first rewriting the source into three pieces: $\mathrm{SW}(\tilde{h},\tilde{u}^1,\tilde{u}^2) = \Psi^0 + \Psi^1 + \Psi^2$, where

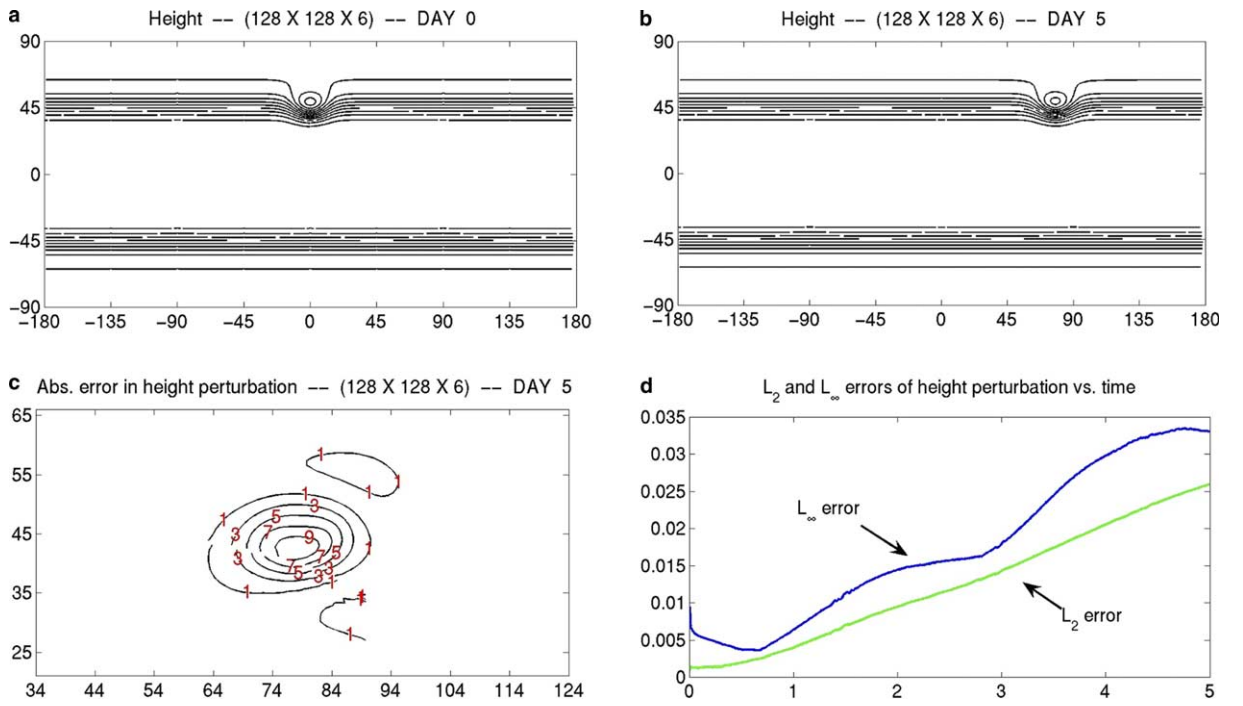

Fig. 8. Williamson et al. [61] Test Case 4 – forced non-linear system with a translating low. Shown in these panels are (a) contours of height on day 0, (b) contours of height on day 5, (c) the absolute error in the height perturbation on day 5, and (d) the time traces of the L_2 and L_∞ errors in the height perturbation as a function of time. The simulation that produced these plots was done on a $128 \times 128 \times 6$ grid. The contour levels are from 10,150 to 10,600 m in increments of 50 m. The 10,150 m contour line is the circle closest to the center of the low.

$$\Psi^0 = \frac{\partial}{\partial t}\left(\sqrt{G}\begin{bmatrix}\tilde{h}\\ \tilde{h}\tilde{u}^1\\ \tilde{h}\tilde{u}^2\end{bmatrix}\right), \quad \Psi^m = \frac{\partial}{\partial x^m}\left(\sqrt{G}\begin{bmatrix}\tilde{h}\tilde{u}^m\\ \tilde{h}\tilde{u}^1\tilde{u}^m + \frac{1}{2}g\tilde{h}^2 G^{1m}\\ \tilde{h}\tilde{u}^2\tilde{u}^m + \frac{1}{2}g\tilde{h}^2 G^{2m}\end{bmatrix}\right).$$

In the expression for Ψ^m, no summation is implied on the index m. Ψ^0 is handled through Strang operator splitting; the resulting ODEs can be solved exactly. The Ψ^1 and Ψ^2 source terms are incorporated into the Riemann problems using the source term strategy of Bale et al. [3]. Simulation results on this problem on a $128 \times 128 \times 6$ are presented in Fig. 8. The errors presented in panels (c) and (d) are errors in the height perturbation only (see Williamson et al. [61] for more details). These results show roughly the same accuracy as those reported by Jablonowski [31] (pp. 145–146).

5.6. Flow over an isolated mountain

Problem #5 in the Williamson et al. test suite modifies the basic shallow water system by adding a compactly supported, conical mountain to the flow. In this problem, the source term due to variable bottom topography is active and is incorporated into the Riemann problems at cell edges by using the source term strategy of Bale et al. [3]. This avoids having to perform operator splitting on the topographic source term; and furthermore, we have found that this treatment improves the conservation of potential enstrophy properties of the scheme.

In this example, the initial total height, $H = h + b$, is the same as that in the Williamson et al. Test Case #2 and the initial velocity is purely zonal with a magnitude of 20 m/s. Without the mountain, this flow would be in geostrophic equilibrium; however, with the mountain an unsteady flow develops. The results of a simulation on a $128 \times 128 \times 6$ grid are presented in Fig. 9. The first three panels ((a)–(c)) show the flow after 5, 10, and 15 days, respectively, while the final panel shows the numerical conservation of mass, total

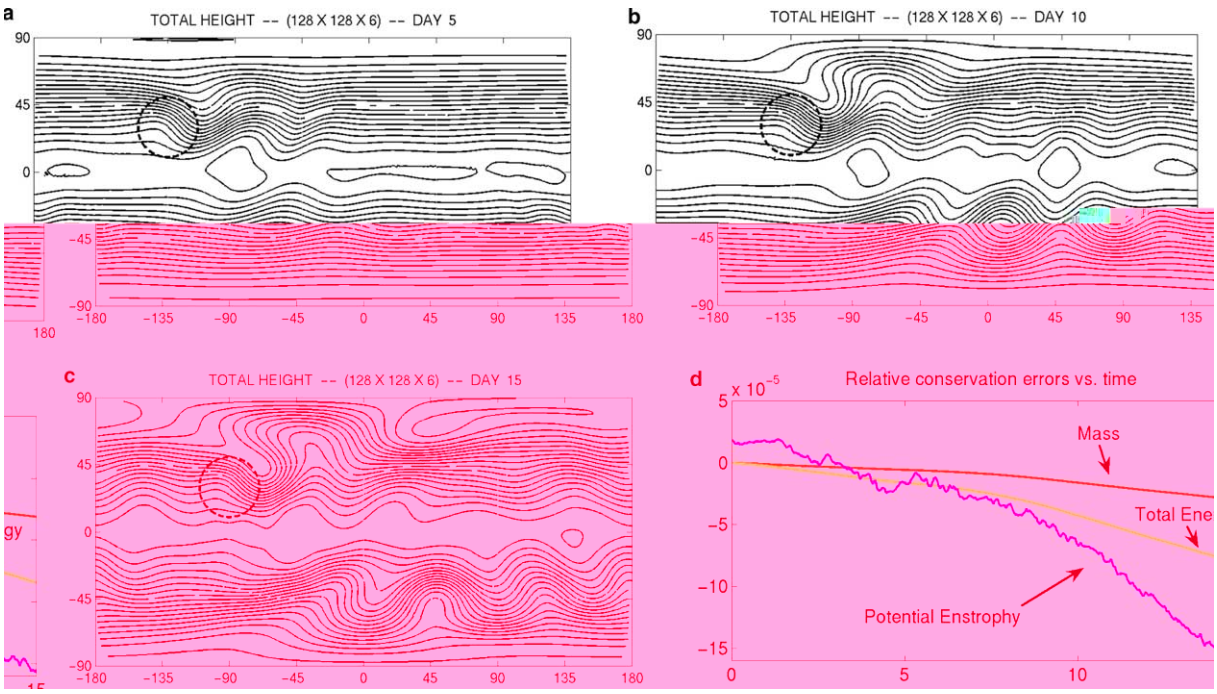

Fig. 9. Williamson et al. [61] Test Case 5 – flow over an isolated mountain. Shown in panels (a)–(c) are the total height at day 5, 10, and 15 on a $128 \times 128 \times 6$ grid. The dashed circle in these plots indicates the location of the conical mountain. The contour levels are from 5000 to 5950 m in increments of 50 m. The two "open" contour lines nearest the equator are at 5900 m, while the closed contour lines on the equator are at 5950 m. The relative conservation errors for conservation of mass, total energy, and potential enstrophy are shown in panel (d).

energy, and potential enstrophy. All of these results are consistent with results in the literature (see for example Jablonowski [31]).

5.7. Rossby–Haurwitz wave

Problem #6 of Williamson et al. [61] involves simulating a global wave structure that propagates parallel to the equator. The initial RH wave can be given any wave number; we refer the reader to formulas (141)–(149) of Williamson et al. [61] for the precise form of the initial conditions. In this test case, a wave number four Rossby–Haurwitz wave is chosen. The results of the proposed wave propagation method on a $128 \times 128 \times 6$ grid at various times are shown in Fig. 10. The first three panels ((a)–(c)) show that the solution computed with the proposed method at relatively early times are in agreement the solutions predicted in the literature (see for example Jablonowski [31]).

On longer time scales, Thuburn and Li [57] showed through numerical simulations that the wave number four Rossby–Haurwitz wave is unstable. In order to compare with their results, we ran our simulation out to longer time. We find that an instability eventually breaks the wave number four symmetry on approximately day 141 of

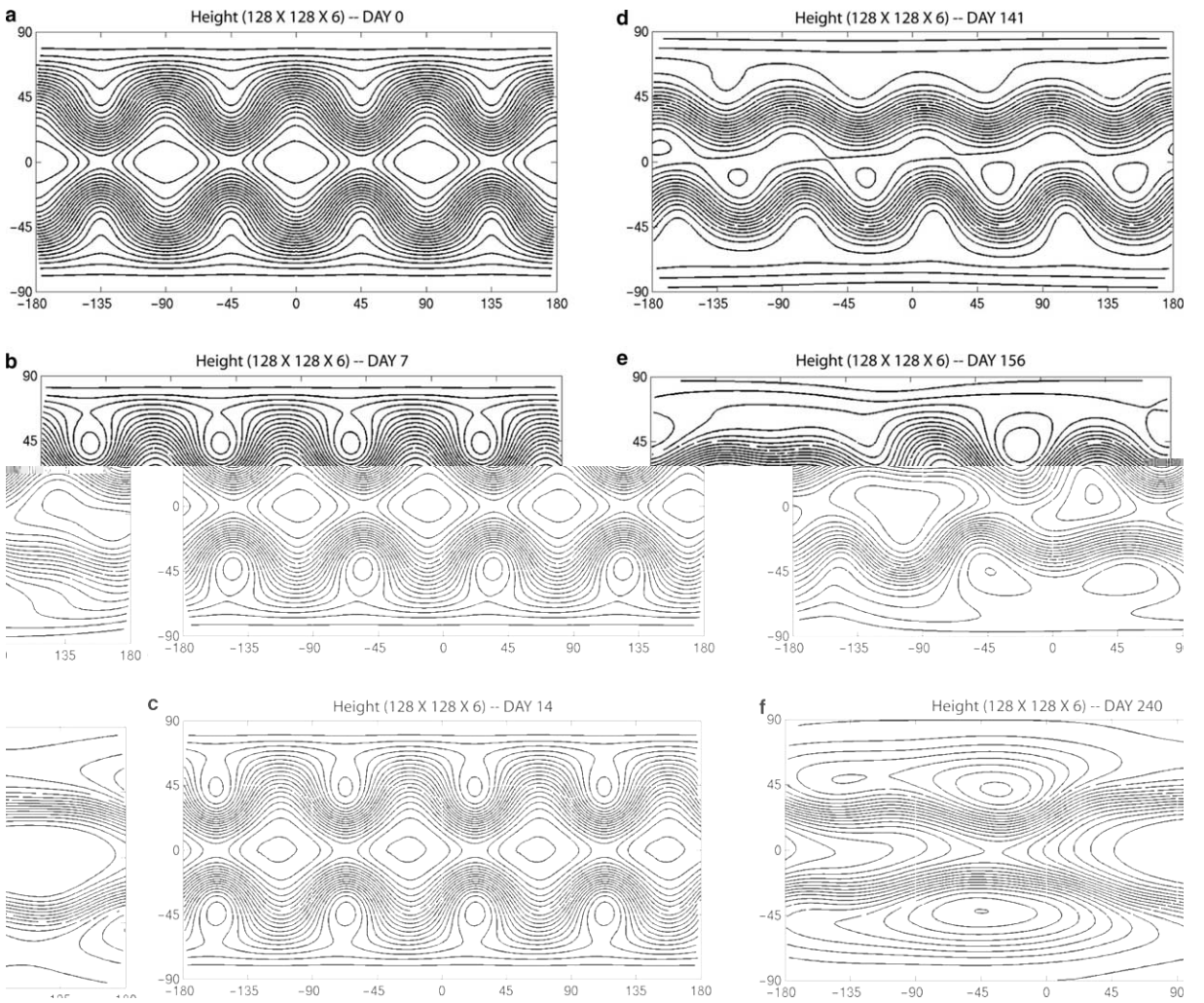

Fig. 10. Williamson et al. [61] Test Case 6 – wavenumber four Rossby–Haurwitz wave. The solution is computed on a $128 \times 128 \times 6$ grid on day (a) 0, (b) 7, (c) 14, (d) 141, (e) 156, and (f) 240. Plots (a)–(c) show the solution at the Williamson et al. [61] test case times. Plots (d)–(f) show the wavenumber four breakdown and subsequent dynamics. The contour levels are from 8100 to 10,500 m in increments of 120 m. The 10,500 m contour lines are the innermost contours, while the 8100 m contour lines are the ones closest to the poles.

the simulation (see panels (d)–(f) of Fig. 10). The breakdown time that we predict is later than the latest time, 100 days, predicted by Thuburn and Li [57]. Thuburn and Li [57] speculated that the details of the instability, including the time at which the wavenumber four symmetry is broken, depends heavily on the numerical truncation error of the scheme, and our results in comparison to their results is an agreement with this observation. We also ran the Rossby–Haurwitz wave problem with grid resolutions of $64 \times 64 \times 6$ and $32 \times 32 \times 6$. The $32 \times 32 \times 6$ simulation showed no signs of an instability even after 240 days; in this case the unstable mode was suppressed by the truncation errors. On the other hand, the $64 \times 64 \times 6$ simulation resembled the $128 \times 128 \times 6$ simulation, and again showed a wave number four symmetry breaking sometime around day 141.

5.8. Unstable jet problem of Galewsky et al. [19]

Next we consider the test case proposed by Galewsky et al. [19]. In this example, a compactly supported, geostrophically balanced jet is placed at a latitude of 45°. This jet is then perturbed by a localized height disturbance, which causes the global jet structure to go unstable. As pointed out by Galewsky et al. [19], this example is quite challenging for second-order methods, since the solution has both a large-scale structure (the jet) as well as fine scale structures that develop due to the perturbation. Therefore, in order to get accurate solutions on this problem without using adaptive mesh refinement techniques, we decompose the total conserved variables into a steady geostrophic and an unsteady part

$$\left(h, u^1, u^2\right) = \left(h_0(\vec{x}), u_0^1(\vec{x}), u_0^2(\vec{x})\right) + \left(\tilde{h}(\vec{x}, t), \tilde{u}^1(\vec{x}, t), \tilde{u}^2(\vec{x}, t)\right).$$

The geostrophically balanced terms are eliminated from the evolution equations, allowing accurate resolution of the unstable perturbations. Following Galewsky et al. [19], we consider two simulations: an inviscid ($\nu = 0$) and a viscous calculation ($\nu = 2.1285 \times 10^{-4}$). The viscous source term can be written as

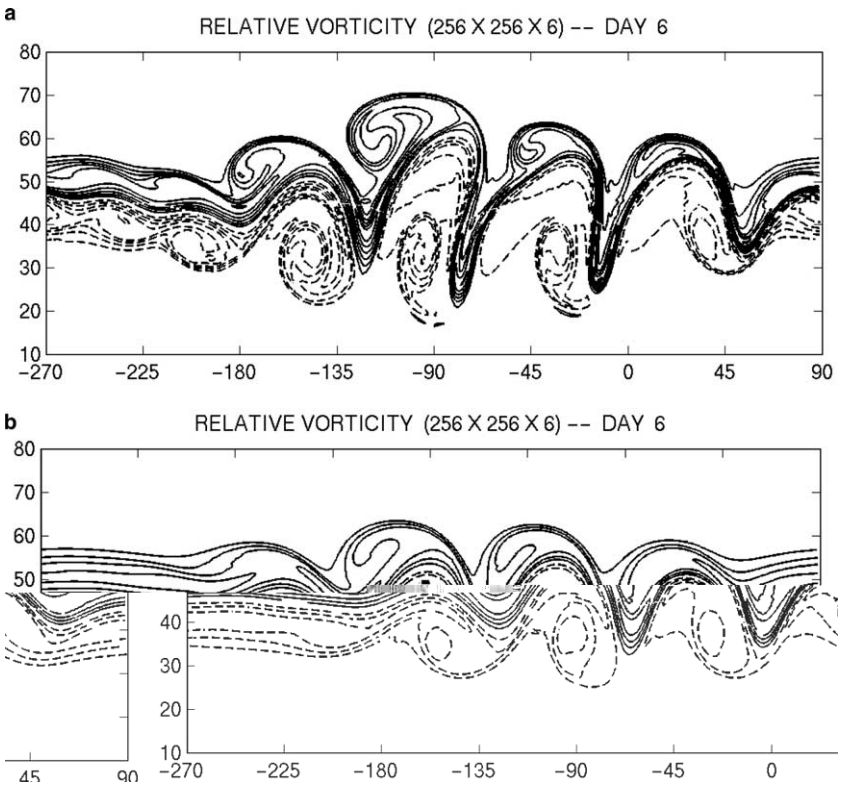

Fig. 11. The unstable jet problem of Galewsky et al. [19]. The solution is displayed at $t = 6$ days on a $256 \times 256 \times 6$ grid with a non-dimensional viscosity of (a) $\nu = 0$ and (b) $\nu = 2.1285 \times 10^{-4}$. The solid contour lines range from $2e-5$ to $3.6e-4$ in increments of $2e-5$, while the dashed contour lines range from $-3.6e-4$ to $-2e-5$ in increments of $-2e-5$ (all numbers in non-dimensional vorticity units).

$$\Psi_D = \left[v\nabla^2 h, v\left(h\nabla^2 u^1 + u^1\nabla^2 h\right), v\left(h\nabla^2 u^2 + u^2\nabla^2 h\right)\right], \tag{35}$$

where

$$\nabla^2 = \frac{1}{\sqrt{G}}\frac{\partial}{\partial x^1}\left(G_{22}\frac{\partial}{\partial x^1} - G_{12}\frac{\partial}{\partial x^2}\right) + \frac{1}{\sqrt{G}}\frac{\partial}{\partial x^2}\left(G_{11}\frac{\partial}{\partial x^2} - G_{12}\frac{\partial}{\partial x^1}\right). \tag{36}$$

Simulation results on a $256 \times 256 \times 6$ grid are shown in Fig. 11. Only small scale differences in the region between $\lambda = -270$ and $\lambda = -225$ are evident between the simulations presented here and those of Galewsky et al. [19]. We note that accurate results are obtained despite the fact that the jet lies directly on top of the grid interfaces between the North Pole grid and the four equatorial patches.

5.9. Longitudinally symmetric shock wave–shallow water equations

In our next example, we consider only the non-rotating shallow water equations ($\Omega = f = 0$). The characteristic length scale for this problem is still the radius of the Earth (6,371,220 m), but now the characteristic time scale is 806.05 s, which is chosen so that the non-dimensional gravitational constant is $g = 1$.

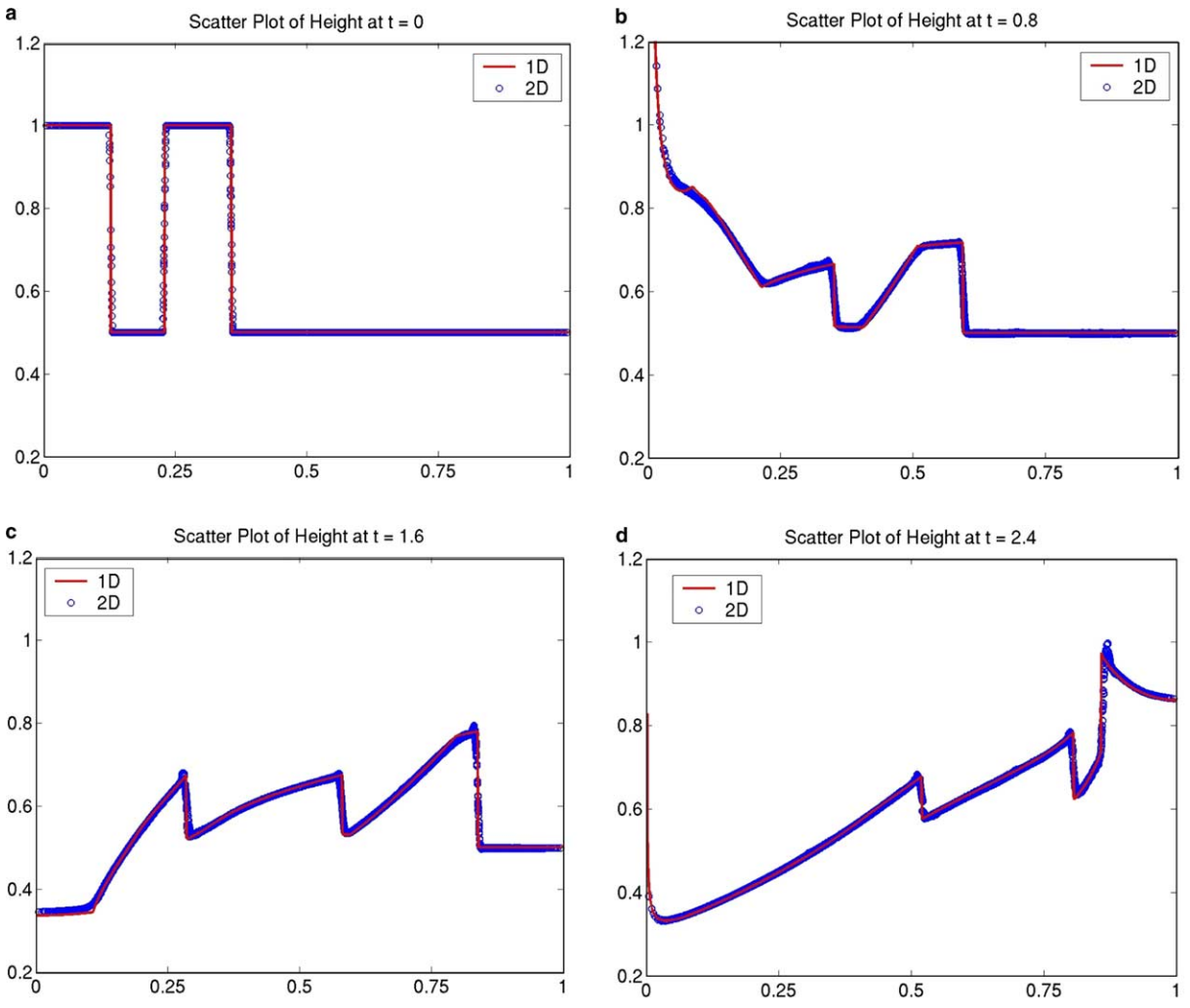

Fig. 12. Zonally symmetric shallow water flow with a discontinuous initial condition. Shown in each plot are a scatter plot of the height from an $80 \times 80 \times 6$ 2D solution on the cubed sphere along with a highly resolved (5000 points) 1D solution. The x-axis in these plots represents the normalized distance from the North Pole; 0 is the North Pole and 1 is the South Pole.

The initial condition consists of a stationary "target" profile centered on the North Pole:

$$h(\lambda,\theta) = \begin{cases} 1 & \text{if } \operatorname{dist}(\lambda,\theta,0,\pi/2) < 0.4, \\ 1 & \text{if } 0.72 < \operatorname{dist}(\lambda,\theta,0,\pi/2) < 1.12, \\ 0.5, & \text{otherwise.} \end{cases}$$

$$u^{\lambda}(\lambda,\theta) = u^{\theta}(\lambda,\theta) = 0.$$

We note that a similar problem was considered by Liska and Wendroff [40]. A scatter plot of the time evolution is shown in Fig. 12; the horizontal axis in these plots is the rescaled latitude, $s = (\pi - 2\lambda)/(2\pi)$, where $s = 0$ and $s = 1$ are the North and South Poles, respectively. For comparison, we also present a highly resolved solution (5000 points) of the 1D longitudinally symmetric shallow water equations:

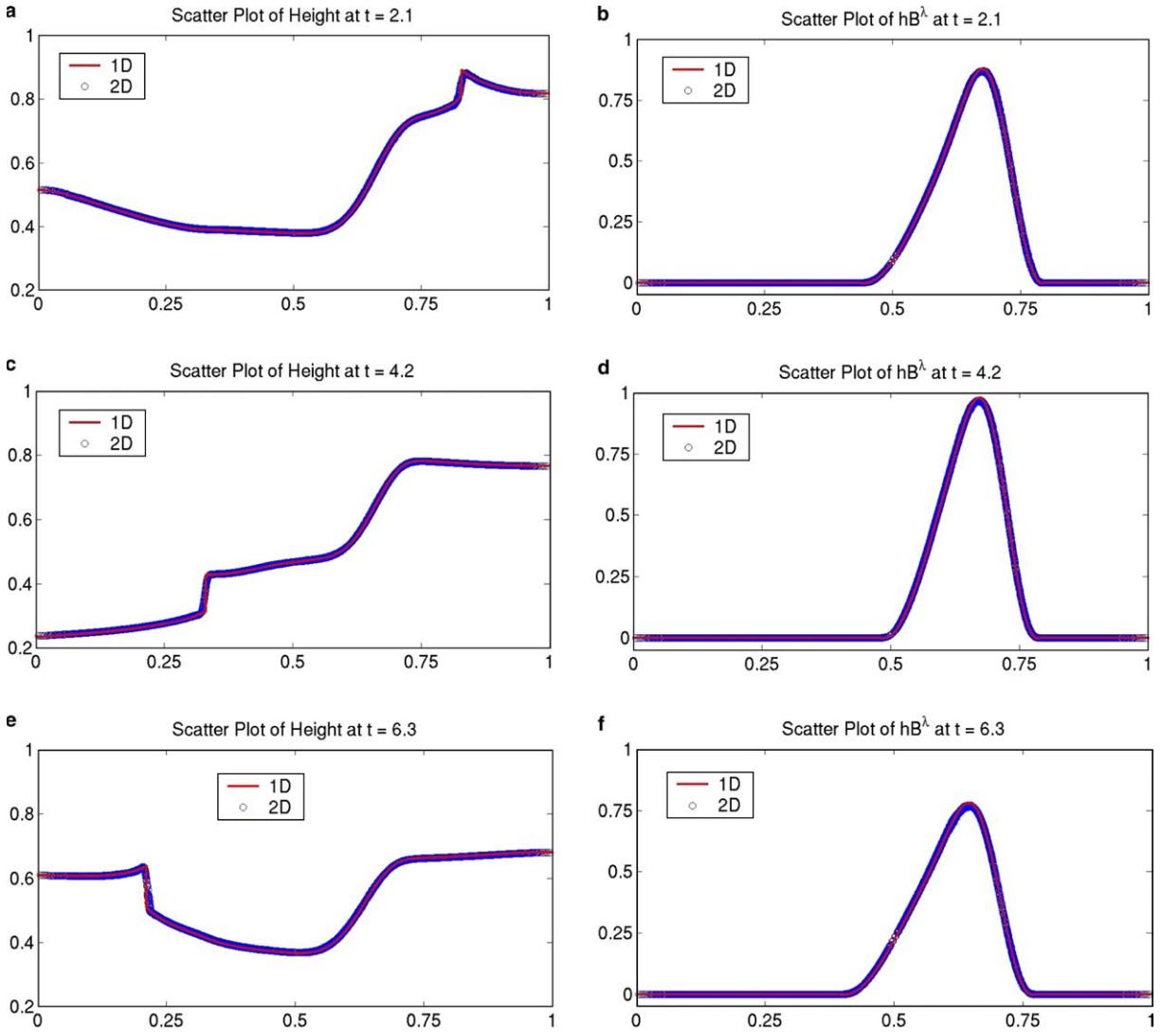

Fig. 13. A symmetric SMHD shock propagation problem using the wave propagation method with constrained transport. Shown in these panels are scatter plots of the heights and hB^{λ} at time (a)–(b) $t = 2.1$, (c)–(d) $t = 4.2$, and (e)–(f) $t = 6.3$. This computation was carried out on an $80 \times 80 \times 6$ grid and compared against a highly resolved (5000 points) 1D simulation. The x-axis in these plots represents the normalized distance from the North Pole; 0 is the North Pole and 1 is the South Pole. Note that ALL of the 2D data is shown in the scatter plot, not just zonal mean values.

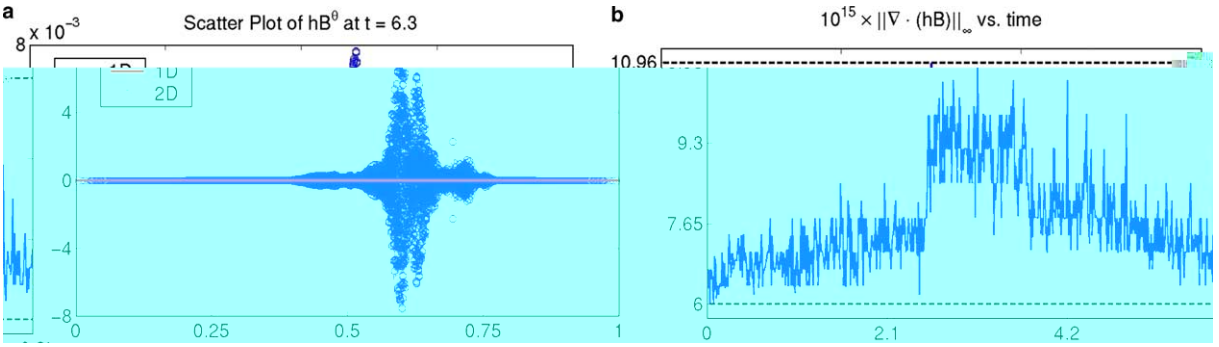

Fig. 14. A symmetric SMHD shock propagation problem using the wave propagation method with constrained transport. Shown in these plots are (a) the scatter plot of hB^θ at the final time $t = 6.3$ and (b) $\|\vec{\nabla}\cdot(h\vec{B})\|_\infty$ (max-norm over entire sphere) as a function of time. Note that ALL of the 2D data is shown in the scatter plot, not just the zonal mean value.

$$\frac{\partial}{\partial t}\begin{bmatrix} h \\ hu^\lambda \\ hu^\theta \end{bmatrix} + \frac{\partial}{\partial \theta}\begin{bmatrix} hu^\theta \\ hu^\lambda u^\theta \\ hu^\theta u^\theta + \frac{1}{2}h^2 \end{bmatrix} = \tan(\theta)\begin{bmatrix} hu^\theta \\ 3hu^\lambda u^\theta \\ hu^\theta u^\theta - \cos^2(\theta) hu^\lambda u^\lambda \end{bmatrix}.$$

Both the 1D (solid line) and the 2D (open circles) results are shown in Fig. 12. These plots indicate that the 2D results are accurate and that they maintain the symmetry of the exact solution. We also note that shock waves propagate through the internal boundaries and corner points without loss of shock-capturing ability or symmetry.

5.10. Longitudinally symmetric shock wave–SMHD equations

Finally, we apply the proposed wave propagation method to a longitudinally symmetric problem for the SMHD equations. We take as initial conditions:

$$h(\lambda,\theta) = 0.5, \quad u^\lambda(\lambda,\theta) = u^\theta(\lambda,\theta) = 0, \quad \mathbb{A}(\lambda,\theta) = \begin{cases} \left(\frac{3}{4} - \frac{66}{\pi^2}\right)s^2 + \frac{1836}{\pi^4}s^4 - \frac{15552}{\pi^6}s^6 & \text{if } -\frac{\pi}{6} < s < \frac{\pi}{6}, \\ 0, & \text{otherwise,} \end{cases}$$

where $s = \mathrm{dist}(\lambda,\theta,0,\pi/2) - 9\pi/16$. We again non-dimensionalize the system so that $g = 1$. These initial conditions are chosen because the initial magnetic field is responsible for kicking-off the subsequent dynamics. The results of a computation on an $80\times 80\times 6$ grid are shown in Fig. 13. We again compare the full 2D solution against a highly resolved 1D solution (5000 points) of the symmetric SMHD equations;

$$\frac{\partial}{\partial t}\begin{bmatrix} h \\ hu^\lambda \\ hu^\theta \\ hB^\lambda \end{bmatrix} + \frac{\partial}{\partial \theta}\begin{bmatrix} hu^\theta \\ hu^\lambda u^\theta \\ hu^\theta u^\theta + \frac{1}{2}h^2 \\ hu^\theta B^\lambda \end{bmatrix} = \tan(\theta)\begin{bmatrix} hu^\theta \\ 3hu^\lambda u^\theta \\ hu^\theta u^\theta - h\cos^2(\theta)(u^\lambda u^\lambda - B^\lambda B^\lambda) \\ hu^\theta B^\lambda \end{bmatrix},$$

where $hB^\theta = 0$ for all space and time. These plots verify that the proposed method accurately captures the shock dynamics generated by the initial magnetic field and maintains the solution symmetry. Furthermore, Fig. 14(a) shows that $hB^\theta = 0$ is maintained to the order of the truncation error, and Fig. 14(b) shows that the discrete divergence of the magnetic field over the entire sphere is maintained to machine precision.

6. Conclusions and future work

This work was concerned with developing an accurate and efficient numerical method for the solution of hyperbolic systems on the sphere. In particular, we focused on developing a method that produces accurate results for both smooth and discontinuous solutions. Numerical solutions of the advection and shallow water

equations from geophysical fluid dynamics and the shallow water magnetohydrodynamic equations from solar physics were presented. All three systems were solved on the cubed sphere grid of Ronchi et al. [49], which covers the sphere with six grid patches that are nearly uniform in grid cell resolution.

Numerical computations on a set of ten test cases showed that the proposed scheme is accurate for a wide range of initial data. Second-order accuracy was verified on examples for the advection and shallow water equations. Three examples with discontinuous solutions were considered, one for each of the three systems. In all the examples, numerical noise from the internal boundaries of the cubed sphere did not significantly influence the overall solution.

Future work will focus on incorporating adaptive mesh refinement (AMR) techniques in order to improve the accuracy and efficiency of the proposed numerical method. This work will follow in the spirit of Berger and Oliger [7]. AMR within a single grid patch can be handled straightforwardly in the wave propagation framework using the ideas presented in Berger and LeVeque [6]. The main challenge will be to handle grids that move from one grid patch to another, since both the indexing and the underlying coordinate system changes across internal boundaries.

Acknowledgments

I would like to thank Randy LeVeque for many fruitful discussions regarding this project. Also, I would like to thank the anonymous reviewers whose comments greatly improved the quality of this paper. The author was partially funded by the NSF VIGRE programs at the Universities of Washington and Michigan and NSF Grant DMS-0106511.

References

[1] R. Abgrall, S. Karni, Computations of compressible multifluids, J. Comput. Phys. 169 (2001) 594–623.
[2] D.S. Bale, Wave Propagation Algorithms on Curved Manifolds with Applications to Relativistic Hydrodynamics, Ph.D. Thesis, University of Washington, Seattle, Washington, 2002.
[3] D.S. Bale, R.J. LeVeque, S. Mitran, J.A. Rossmanith, A wave propagation method for conservation laws and balance laws with spatially varying flux functions, SIAM J. Sci. Comp. 24 (2003) 955–978.
[4] J.M. Bardeen, L.T. Buchman, Numerical tests of evolution systems, gauge conditions, and boundary conditions for 1d colliding gravitational plane waves, Phys. Rev. D 65 (2002).
[5] J. Behrens, An adaptive semi-Lagrangian advection scheme and its parallelization, Mon. Weather Rev. 124 (1996) 2386–2395.
[6] M.J. Berger, R.J. LeVeque, Adaptive mesh refinement using wave propagation algorithms for hyperbolic systems, SIAM J. Numer. Anal. 35 (1998) 2298–2316.
[7] M.J. Berger, J. Oliger, Adaptive mesh refinement for hyperbolic partial differential equations, J. Comput. Phys. 53 (1984) 484–512.
[8] R. Blikberg, Nested Parellelism in Open MP with Application to Adaptive Mesh Refinement, Ph.D. Thesis, University of Bergen, Norway, 2003.
[9] W. Bourke, An efficient, one-level, primitive-equation spectral model, Mon. Weather Rev. 100 (1972) 683–698.
[10] J.U. Brackbill, D.C. Barnes, The effect of nonzero $\nabla \cdot b$ on the numerical solution of the magnetohydrodynamic equations, J. Comput. Phys. 35 (1980) 426–430.
[11] J. Côté, A. Staniforth, An accurate and efficient finite-element global model of the shallow-water primitive equations, Mon. Weather Rev. 118 (1990) 2707–2717.
[12] G. Chesshire, W.D. Henshaw, Composite overlapping meshes for the solution of partial-differential equations, J. Comput. Phys. 90 (1990) 1–64.
[13] A.J.C. de Saint-Venant, Théorie du mouvement non-permanent des eaux, avec crues des rivière et à l'introduction des marées dans leur lit, CR Acad. Sci. Paris 73 (1871) 147–154.
[14] C. Evans, J.F. Hawley, Simulation of magnetohydrodynamic flow: a constrained transport method, Astrophys. J. 332 (1988) 659.
[15] T. Fogarty, Finite Volume Methods for Acoustics and Elasto-plasticity with Damage in a Heterogeneous Medium, Ph.D. Thesis, University of Washington, Seattle, Washington, 2002.
[16] T.R. Fogarty, High-resolution Finite Volume Methods for Acoustics in a Rapidly-varying Heterogeneous Medium, Master's Thesis, University of Washington, Seattle, Washington, 1997.
[17] T.R. Fogarty, R.J. LeVeque, High-resolution finite volume methods for acoustics in periodic and random media, J. Acoust. Soc. Am. 106 (1) (1999) 1–12.
[18] A. Fournier, M.A. Taylor, J.J. Tribbia, The spectral element atmosphere model (SEAM): high-resolution parallel computation and localized resolution of regional dynamics, Mon. Weather Rev. 132 (2004) 726–748.
[19] J. Galewsky, R.K. Scott, L.M. Polvani, An initial-value problem for testing numerical models of the global shallow-water equations, Tellus 56A (2004) 429–440.

[20] P.A. Gilman, Magnetohydrodynamic "shallow water" equations for the solar tachocline, Astrophys. J. 544 (2000) L79–L82.
[21] F.X. Giraldo, Lagrange–Galerkin methods on spherical geodesic grids: the shallow water equations, J. Comput. Phys. 160 (2000) 336–368.
[22] F.X. Giraldo, A spectral element shallow water model spherical geodesic grids, Int. J. Numer. Meth. Fluid 35 (2001) 869–901.
[23] F.X. Giraldo, J.S. Hesthaven, T. Warburton, Nodal high-order discontinuous Galerkin methods for the spherical shallow water equations, J. Comput. Phys. 181 (2002) 499–525.
[24] F.X. Giraldo, T.E. Rosmond, A scalable spectral element Eulerian atmospheric model (SEE-AM) for NWP: dynamical core tests, Mon. Weather Rev. 132 (2004) 133–153.
[25] R. Heikes, D.A. Randall, Numerical integration of the shallow water equations on a twisted icosahedral grid. Part I: Basic design and results of tests, Mon. Weather Rev. 123 (1995) 1862–1880.
[26] R. Heikes, D.A. Randall, Numerical integration of the shallow water equations on a twisted icosahedral grid. Part II: A detailed description of the grid and an analysis of numerical accuracy, Mon. Weather Rev. 123 (1995) 1881–1887.
[27] C. Helzel, Numerical Approximation of Conservation Laws with Stiff Source Terms for the Modelling of Detonation Waves, Ph.D. Thesis, Otto-von-Guericke-Universität Magdeburg, Magdeburg, Germany, 2000.
[28] C. Helzel, R.J. LeVeque, G. Warnecke, A modified fractional step method for the accurate approximation of detonation waves, SIAM J. Sci. Comp. 22 (2000) 1489–1510.
[29] S.D. Hern, J.M. Stewart, The Gowdy T-3 cosmologies revisited, Classic. Quant. Grav. 15 (1998) 1581–1593.
[30] M.E. Hubbard, N. Nikiforakis, A three-dimensional, adaptive, Godunov-type model for global atmospheric flows, Mon. Weather Rev. 131 (2003) 1848–1864.
[31] C. Jablonowski, Adaptive Grids in Weather and Climate Modeling, Ph.D. Thesis, University of Michigan, Ann Arbor, 2004.
[32] J.D. Jackson, Classical Electrodynamics, third ed., Wiley, New York, 1999.
[33] J.O. Langseth, R.J. LeVeque, A wave propagation method for three-dimensional hyperbolic conservation laws, J. Comput. Phys. 165 (2000) 126–166.
[34] D. Lanser, J.G. Blom, J.G. Verwer, Time integration of the shallow water equations in spherical geometry, J. Comput. Phys. 171 (2001) 373–393.
[35] R.J. LeVeque, D.H. Yong, Solitary waves in layered nonlinear media, SIAM J. Appl. Math. 63 (2003) 1539–1560.
[36] R.J. LeVeque, High-resolution conservative algorithms for advection in incompressible flow, SIAM J. Numer. Anal. 33 (1996) 627–665.
[37] R.J. LeVeque, Wave propagation algorithms for multi-dimensional hyperbolic systems, J. Comput. Phys. 131 (1997) 327–335.
[38] R.J. LeVeque, Finite Volume Methods for Nonlinear Elasticity in Heterogeneous Media, in: Proceedings of the ICFD Conference on Numerical Methods for Fluid Dynamics, 2001.
[39] R.J. LeVeque, Finite Volume Methods for Hyperbolic Problems, Cambridge University Press, Cambridge, 2002.
[40] R. Liska, B. Wendroff, Shallow water conservation laws on a sphere, in: H. Freistühler, G. Warnecke (Eds.), International Series of Numerical Mathematics, vol. 141, Birkhauser Verlag, Basel, 2001, pp. 673–682.
[41] J. McGregor, Semi-Lagrangian advection on conformal cubic grids, Mon. Weather Rev. 124 (1996) 1311–1322.
[42] C.W. Misner, K.S. Thorne, J.A. Wheeler, Gravitation, W.H. Freeman, San Fransisco, 1973.
[43] R.D. Nair, S.J. Thomas, R.D. Loft, A discontinuous Galerkin global shallow water model, Mon. Weather Rev. 133 (2005) 876–888.
[44] R.D. Nair, S.J. Thomas, R.D. Loft, A discontinuous Galerkin transport scheme on the cubed sphere, Mon. Weather Rev. 133 (2005) 814–828.
[45] T. Nihei, K. Ishii, A fast solver for the shallow water equations on a sphere using a combined compact difference scheme, J. Comput. Phys. 187 (2003) 639–659.
[46] J. Pedlosky, Geophysical Fluid Dynamics, second ed., Springer, Berlin, 1987.
[47] R.J. Purser, M. Rancic, Smooth quasi-homogeneous gridding of the sphere, J. Comput. Phys. 124 (1998) 637–647.
[48] M. Rancic, R.J. Purser, F. Mesinger, A global shallow-water model using an expanded spherical cube: Gnomonic versus conformal coordinates, Q. J. Roy. Meteor. Soc. 122 (1996) 959–982.
[49] C. Ronchi, R. Iacono, P.S. Paolucci, The 'cubed sphere': a new method for the solution of partial differential equations in spherical geometry, J. Comput. Phys. 124 (1996) 93–114.
[50] J.A. Rossmanith, An unstaggered, high-resolution constrained transport method for magnetohydrodynamic flows, SIAM J. Sci. Comp. (submitted). Available from: <http://www.math.lsa.umich.edu/~rossmani/preprints/mhdpaper.pdf>.
[51] J.A. Rossmanith, D.S. Bale, R.J. LeVeque, A wave propagation algorithm for hypberbolic systems on curved manifolds, J. Comput. Phys. 199 (2004) 631–662.
[52] R. Sadourny, Conservative finite-difference approximations of the primitive equations on quasi-uniform spherical grids, Mon. Weather Rev. 100 (1972) 211–224.
[53] W.F. Spotz, M.A. Taylor, P.N. Swarztrauber, Fast shallow-water equation solvers in latitude–longitude coordinates, J. Comput. Phys. 145 (1998) 432–444.
[54] H. De Sterck, Hyperbolic theory of the "shallow water" magnetohydrodynamics equations, Phys. Plasmas 8 (7) (2001) 3293–3304.
[55] G. Tóth, The $\nabla \cdot B = 0$ constraint in shock-capturing magnetohydrodynamics codes, J. Comput. Phys. 161 (2000) 605–652.
[56] J. Thuburn, A PV-based shallow-water model on a hexagonal–icosahedral grid, Mon. Weather Rev. 125 (1997) 2328–2347.
[57] J. Thuburn, Y. Li, Numerical simulations of Rossby–Haurwitz waves, Tellus 52A (2000) 181–189.
[58] M.A. Tolstykh, Vorticity-divergence semi-Lagrangian shallow-water model on the sphere based on compact finite differences, J. Comput. Phys. 179 (2002) 180–200.

[59] H. Tomita, M. Tsugawa, M. Satoh, K. Goto, Shallow water model on a modified icosahedral geodesic grid by using spring dynamics, J. Comput. Phys. 174 (2001) 579–613.
[60] B. van Leer, Towards the ultimate conservative difference scheme II. Monotonicity and conservation combined in a second order scheme, J. Comput. Phys. 14 (1974) 361–370.
[61] D.L. Williamson, J.B. Drake, J.J. Hack, R. Jakob, P.N. Swarztrauber, A standard test set for numerical approximations to the shallow water equations in spherical geometry, J. Comput. Phys. 102 (1994) 211–224.